Two-layer gravity inversion on Mars

Three different inversion methods to obtain a global density model of the crust and upper mantle of Mars

Master thesis

Fenna van den Bogaard

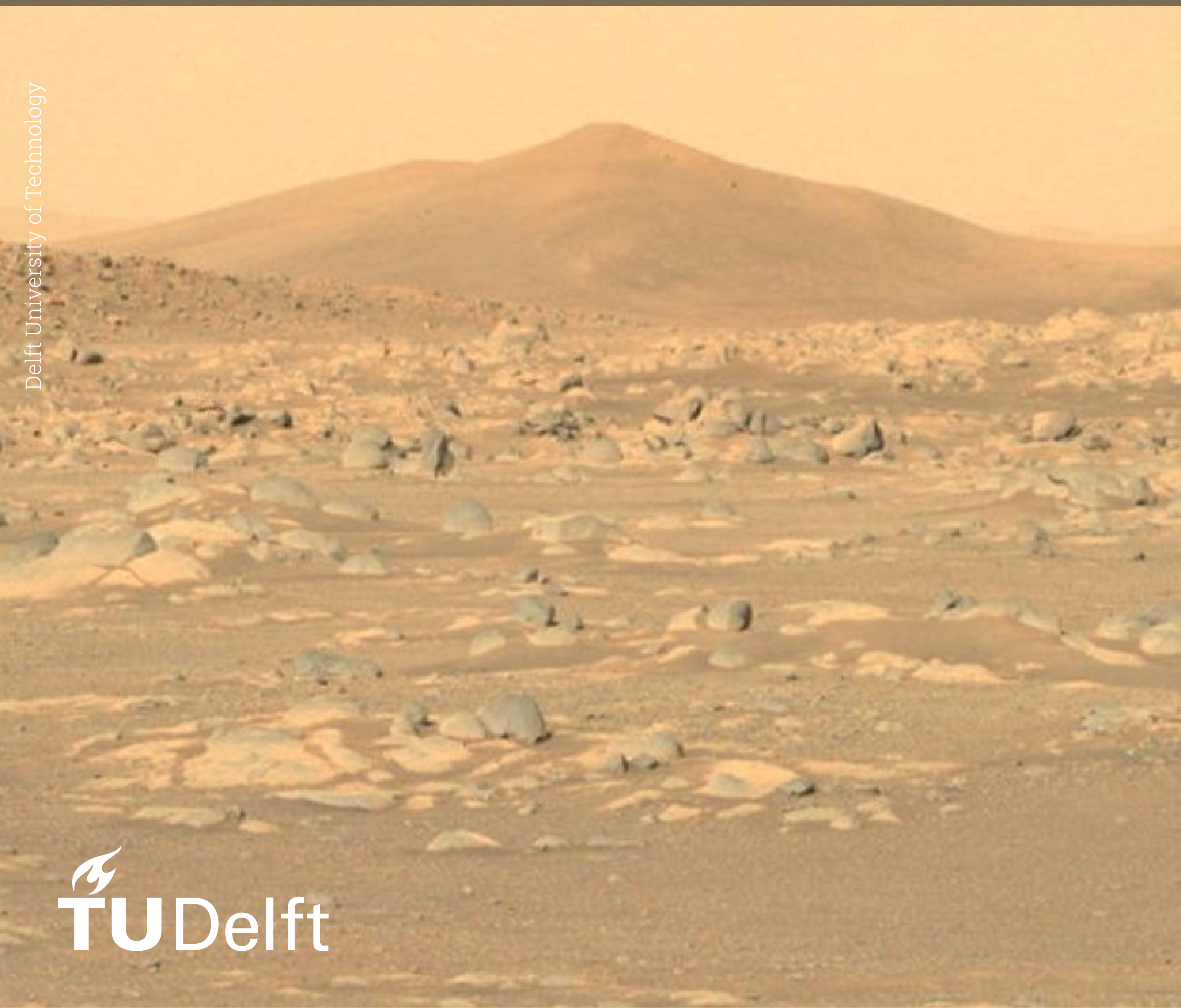

Delft University of Technology

Two-layer gravity inversion on Mars

Three different inversion methods to obtain a global density model of the crust and upper mantle of Mars

by

Fenna van den Bogaard

to obtain the degree of Master of Science
at the Delft University of Technology,
to be defended publicly on Friday April 5, 2024 at 9:15 AM.

Student number:	4678745	
Project duration:	June 6, 2023 – April 5, 2024	
Thesis committee:	Dr. ir. B. C. Root	TU Delft, supervisor
	Dr. ir. W. van der Wal	TU Delft, chair
	J.G. De Teixeira da Encarnacao	TU Delft

Cover image: Mars Perseverance Sol 4: Right Mastcam-Z Camera, on February 22 2021. (Credits: NASA/JPL-Caltech/ASU/MSSS)

TU Delft

Abstract

The origin of the Martian dichotomy is subject to question and no substantial evidence for the origination exists. However, it is of great importance for the understanding of the formation and development of celestial bodies to know more about the Martian geology. Some surface and subsurface features that are not visible in, e.g., topography data, might show up in gravity data. Therefore, this research inverts gravity data to find a global crustal and mantle density model. Previous research performed a one-layer inversion, assuming equal mass in all columns. Furthermore, data from missions like InSight do not provide a global interior model, but only provide information at the landing site. The aim of this research is to provide a global density model of both the Martian crust and upper mantle, in order to better understand the Martian surface characteristics.

The inversion is performed using a weighted, regularized least-squares algorithm. The observations are retrieved from the MRO120F dataset, which combines gravity data from Mars missions like MRO and MGS. The gravity residual that is inverted is computed by subtracting the state-of-the-art gravity field model of the TU Delft from the MRO120F gravity field. The design matrix is built using Green's functions, which define the influence of a mass element in all different directions on a measurement point.

This least-squares method is first applied to a one-layer inversion. From this part of the research, a linear relationship between the optimal combination of the regularization parameter and the weights of the observations was determined. Additionally, it was found that incorporating the correct value for the layer depth is important to retrieve correct results. Other parameters, like the isostasy type of the crust-mantle boundary, are of less importance.

Using the same least-squares algorithm, three different methods for a two-layer inversion are used. The separate two-layer inversion uses the gravity residual to invert first for the crust, computing a new gravity residual and using that to invert the mantle. The combined independent two-layer inversion uses the initial gravity residual to invert the crust and mantle at the same time but parallel to each other. The third method, the combined dependent two-layer inversion, uses a full matrix with the crust and mantle stacked upon each other to invert both layers simultaneously. All three inversion methods are performed on synthetic planets as well.

By performing all inversions on the synthetic planets, it was found that the combined independent two-layer inversion results in a strong decoupling of short and long wavelength signals, but is not able to attribute gravity signals to different features in the crust and mantle. The combined dependent two-layer inversion does lead to a result that shows decoupling of crust and mantle features. The hypothesis is that adding different gravity components to the combined dependent two-layer inversion will further increase its accuracy.

The results of the inversion methods applied to Mars are in agreement with existing research in terms of standard deviations of the crust and mantle density anomalies. The maps were also analysed geologically, where the most important conclusion is the evidence of potential impact basins in the north polar region. These can be evidence to accept the several impacts theory for the origination of the Martian dichotomy. Increasing the resolution and refining the third inversion method with multiple gravity components will increase the potential of gravity inversion to define geological features of Mars.

Preface

When starting this master's thesis, I was curious and excited. How would the upcoming year look like? Would I enjoy it? Working on your own research every day can be tough, having to push yourself day in and day out. Now that this master's thesis is completed and laying before you, I am very proud. I am proud of this research, proud of the process and proud of myself. This document marks the end of a wonderful student life, of which I am still in denial that it will be over in two weeks.

Throughout this process, I had the privilege of being supervised by Bart Root. I would like to express my gratitude for your guidance, which has truly made my research experience enjoyable. Your commitment to spending an hour every week listening to me, answering my questions, and brainstorming with me was admirable. In addition to the weekly meetings, you always took the time to answer my questions and your door was always open. I think few supervisors are as consistently involved in their students' projects as you are. Our communication was pleasant and I felt that you took me seriously. I highly recommend any student to graduate with you!

I would also like to thank my fellow thesis students in room NB2.56 at the AE faculty for making this time of working on my own enjoyable. Maintaining contact with friends and being able to discuss each other's highs and lows is invaluable, and I wish all students had this support.

Then, there are lots of other people that I want to thank, not only for supporting me during this thesis, but during the last 6.5 years. My student life has been amazing and I owe it all to my study friends, teammates, (former) roommates, fellow board members, my boyfriend, my parents and sister, and all the other people I have met on the way.

As I begin the next, still unknown, chapter of my life, I will forever cherish my time at the TU Delft.

Fenna van den Bogaard
Delft, March 2024

Contents

Abstract i

Preface ii

List of Figures iv

List of Tables v

1 Introduction 1
- 1.1 Martian geology and the opportunities of gravity field data 1
- 1.2 Martian interior 4
- 1.3 Gravity and spherical harmonics 6
- 1.4 Research aim and research question 7
- 1.5 Report outline 8

2 Preliminary study: One-layer inversion 9
- 2.1 An introduction to the least-squares problem 9
- 2.2 Implementation of the one-layer gravity inversion 11
- 2.3 Sensitivity analysis on λ, σ and satellite height 16

3 Journal article 21

4 Data analysis and verification and validation 36
- 4.1 Verification and validation of data sets and tools 36
  - 4.1.1 Martian topography: MOLA 36
  - 4.1.2 GSH tool 37
  - 4.1.3 Martian gravity: a comparison of different data sets 37
- 4.2 Vertical gravity gradient and anomaly 38
- 4.3 Bouguer anomaly 39
  - 4.3.1 Analytic Bouguer anomaly 40
  - 4.3.2 Non-analytic Bouguer anomaly 41
- 4.4 One-layer inversion 42

5 Conclusions and recommendations 43
- 5.1 Conclusions 43
- 5.2 Recommendations 44

Bibliography 45

List of Figures

1.1 A topographic map of Mars, with the most important features labelled. This figure is created using MOLA data. 2

2.1 An example of an L-curve for a standard ridge regression, where $x_0 = 0$ [Hansen, 2001]. 11
2.2 This figure, obtained from Martinec [2014], shows the isotropic kernels K_{rr}, $K_{r\Omega}$ and $K_{\Omega\Omega}$ as a function of the angular distance ψ and at a height of the computation point of 255 km. For this figure the radius of the Earth is used. . . 13
2.3 A sensitivity analysis of λ and σ on a model with a crust that has a depth of 100 km and a thickness of 100 km. The satellite height of the observations is 200 km. The inversion is performed using the gravitational potential. 17
2.4 The optimal combinations for λ and σ to be used in the weighted, regularized, least-squares problem. Described for all three gravity components. 17
2.5 A qualitative analysis of the effect of a stable and unstable λ-σ combination . . 18
2.6 A height analysis for an inversion using the gravitational potential with $\sigma = 1e-1$, $\lambda = 1e-4$. On the y-axis the root-mean-square of the density error is depicted. Note that it is a logarithmic scale. 19
2.7 A heat map of a one-layer inversion using different values for Te and D_c. Note that the color bar is cut-off at 25 and 100 kg/m^3, and uses a logarithmic scale. . 19

4.1 Validation of MOLA data with Wieczorek [2015] 37
4.2 Degree variance of MRO120F, MRO120D and GMM-3, including their respective errors 38
4.3 Zoomed in version of Figure 4.2, showing the higher degree values for all three data sets. 39
4.4 Vertical gravity gradient and anomaly of Mars using MRO120F 39
4.5 Gravity anomaly of Mars, corrected for C00, C10, C11, S11 and C20 as presented by van Brummen [2022]. It must be noted that both the projection and the central meridian are different. The color map and color bar used is the same. 40
4.6 Analytic Bouguer anomaly with a maximum of 1036 mGal and a minimum of -945 mGal 40
4.7 Non-analytic Bouguer anomaly with a maximum of 1064 mGal and a minimum of -931 mGal 41
4.8 Difference between the analytic and the non-analytic Bouguer anomalies with a maximum of 793 mGal and a minimum of -657 mGal 41
4.9 Results of a one-layer inversion after only one iteration. 42

List of Tables

2.1 Final input values for σ, λ and height of satellite observations to be used in the least-squares algorithm 18

1 Introduction

As early as 1965, NASA's Mariner 4 successfully performed the first flyby of Mars [Sloan, 1968]. Since then, an enormous amount of data has been returned by several spacecraft and landers that are shaping our understanding of Mars. However, much remains unknown. Understanding the interior of Mars is crucial for gaining insight into its origin, development, and the formation of celestial bodies. Therefore, studying the interior of Mars can also enhance our understanding of Earth. Another reason for studying this planet is the potential for life on Mars. Since the first flybys of Mars, scientists have speculated that Mars could support life or be a potential habitat for life due to the possible presence of water. For these reasons, this research aims to enhance our understanding of Mars and its geological history.

The research problem and area will be further introduced in this Chapter. First, section 1.1 elaborates on the geologic history and surface characteristics of Mars, while simultaneously presenting the opportunities of using gravity field data to study the Martian geology. Then, the Martian interior will be introduced in section 1.2. This is split up into research that was conducted before the InSight mission and after the InSight mission. As this research will use gravity field data, section 1.3 explains the basics of gravity and the spherical harmonic representation that is used in this study. Finally, the research question is defined in section 1.4 and section 1.5 elaborates on the outline of the whole report.

1.1. Martian geology and the opportunities of gravity field data

Looking from the Sun, Mars is the fourth planet in an orbit around the Sun. It is the second smallest planet in our solar system, being smaller (in radius) than the Earth. Its seemingly red color is very characteristic and can be distinguished by eye during the night. This red colour is due to the surface of Mars, which consists of oxidized rocks. This oxidized surface layer has iron minerals in it, giving it a red color (like rust). Above this surface layer, only a very thin, airy atmosphere is present. The mean gravity on Mars is around one third of the gravity on Earth, namely 3.72 m/s^2 [Williams, 2004].

The history of Mars can be divided into three main periods [Carr and Head, 2010]. The first of these geologic periods, the Noachian epoch, started around 4.1 GYr and ended around 3.7 GYr ago. The Martian terrain that dates back to the Noachian epoch is characterized by the bombardment era. This results in heavily cratered surface features, covering about 40% of the surface of Mars. Then the Hesperian epoch started. This period dates from 3.7 GYr old to 3 GYr old. The next period is called the Amazonian epoch, dating from 3 GYr ago to present [Carr and Head, 2010].

Before the Noachian period, already a big geological event happened: the global dichotomy. After the fairly quick accretion of Mars after the Solar System formation, Mars' northern and

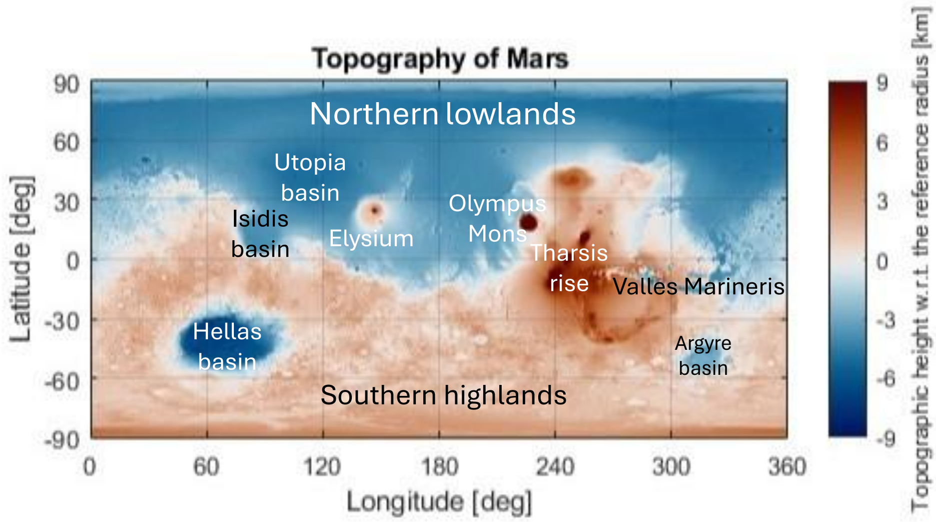

Figure 1.1: A topographic map of Mars, with the most important features labelled. This figure is created using MOLA data.

southern hemispheres started showing differences [Zuber et al., 2000] [Carr and Head, 2010]. The dichotomy boundary is not exactly coinciding with the northern and southern hemisphere, but does follow this approximately, as can be seen in Figure 1.1. The Martian dichotomy is visible in three characteristics. First, the dichotomy is present in the different elevations of the two hemispheres: the southern hemisphere is elevated around 5.5 km more than the northern hemisphere [Aharonson et al., 2001]. The dichotomy is also present in the thickness of the crust: the northern hemisphere seems to have a thinner crust, being around 30 km, than the southern crust, being around 60 km thick [Neumann et al., 2004]. Thirdly, the dichotomy is present in the crater count. The southern hemisphere is more heavily cratered than the north, however it could be the case that the surface north of the dichotomy boundary is covered by younger deposits and therefore showing less cratering. There is still a lot of uncertainty about the time and mode of formation of this dichotomy. Large impacts, global mantle convection or tectonics are all formation theories that are studied, but there is no definite conclusion on this [Carr and Head, 2010]. Also, as Mars is a very active planet it is hard to study the surface conditions during the dichotomy period, as the geologic record has been almost completely erased.

Figure 1.1 shows the main topographic features present on mars. In this map, the dichotomy is clearly present: the elevated topography in the south and on the other hand the northern lowlands. The Tharsis Rise is also very distinct. Accumulated at the end of the Noachian period, Tharsis is a volcanic pile of 9 km high and a diameter of around 5000 km [Philips et al., 2001]. Next to the Tharsis Rise, Olympus Mons is present. This is the biggest and most prominent shield volcano in the Solar System [Mouginis-Mark, 2018]. Impact basins like Hellas and Utopia also leave their marks in the topography of Mars [Frey and Schultz, 1990] [Tanaka and Leonard, 1995].

The origination of the global dichotomy is unclear up until now. Multiple hypotheses or theories about the development of the global dichotomy are present. These can roughly be divided into two types: endogenic processes or large impacts. Within these two types, several theories are again present [Solomon et al., 2001] [Mcgill and Squyres, 1991].

Endogenic processes can entail inconsistent magma heat flows, or plate tectonics. Both of these theories ([Elkins-Tanton et al., 2003], [Sleep, 1994]) agree that the northern hemisphere experienced an upwelling, leading to a thinner crust. Theories that involve large impact are divided: was it one large impact or several smaller impacts? A large impact in the north could create one big impact basin that is now known as the northern lowlands [Wilhelms and Squyres, 1984]. However, the question is if Mars could have survived such a big impact.

Gravity data can be used to study this theory by revealing features such as concentric gravity anomalies that coincide with the proposed large impact basin or, alternatively, find features that prove to be incompatible with this hypothesis. The several impacts theory originates from the expected size distribution of impacts. If one large impact would have occurred, several smaller impacts should also be present. Therefore, Frey and Schultz [1988] discuss that multiple overlapping impacts can explain the global dichotomy.

As is discussed in this section, the Martian dichotomy still serves a lot of questions. Previously, it was assumed that the northern hemisphere was a younger surface due to crater counting. However, with studying the gravity field of Mars, it might be possible to determine geological features like quasi-circular depressions. These quasi-circular depressions (QCD's) are thought to be old craters that have been buried with a layer of sediment. Therefore, they do not show up in topography data, but might show up in gravity data [Buczkowski et al., 2005]. These QCD's are mostly occurring in the northern hemisphere. If these proposed QCD's indeed are buried craters, this changes the crater counting and might show that the northern hemisphere is in fact older than the southern hemisphere.

The impact crater theories for the dichotomy and the QCD's show that by analysis of gravity data, the geology of Mars can be better understood. The observed gravity field is the combination of surface relief, relief along the crust-mantle boundary and relief within the mantle and the core. This allows for a geological interpretation of the gravity field, meaning that the gravity field can reveal geologic processes such as impact craters, volcanism and other subsurface structures [Wieczorek et al., 2022].

Detecting the history of plate tectonics using gravity data is challenging. However, gravity data can be used to identify volcanism and its associated features. Since volcanism is linked to plate tectonics, studying volcanic activity can provide insights into early plate tectonics on Mars. For instance, the Tharsis region, renowned for its extensive volcanic structures, creates gravitational anomalies due to its significant mass. Analyzing gravity data enables the examination of flexure and stress patterns caused by the Tharsis bulge. The formation of the global dichotomy was likely influenced by the tectonic uplift and deformation resulting from these stress patterns. If the gravity data demonstrates connections between Tharsis volcanic features and deformation patterns along the dichotomy boundary, it would support the hypothesis of Tharsis volcanism. Conversely, if the gravity data shows no correlation between Tharsis and dichotomy features, it would challenge this hypothesis. Zuber et al. [2000] has already discussed that the gravity anomalies do not necessarily follow the crustal thickness variations, such that tectonics seem less likely.

The other endogenic process that might be the reason of the global dichotomy is mantle dynamics: upwelling or downwelling creating thinner and thicker crust. Gravity data can reveal variations in the crustal density that are associated with the mantle processes. In order to know if the crustal density variations that are found can indeed be linked to this, first a proposed mantle dynamics history needs to be sketched. For instance, studies (e.g. Neumann et al. [2004], Smrekar et al. [2019]) have revealed that the southern highlands possess a significantly thicker crust compared to the northern lowlands. This discrepancy suggests that processes such as crustal thickening or magmatic intrusions might have contributed to the formation of the dichotomy.

Then, how can gravity data be used to accept or reject the single and several impact hypotheses? The massive single impact event formed the so called Borealis basin. Topography can reveal the shape or shapes of the basins; and the presence of gravity signatures representing basins can be used to explain the northern lowlands. This includes the gravity anomalies associated with every impact basin: a depression surrounded with a circle of relatively high gravity values - the rim. Also, an impact of sufficient magnitude to form the Borealis Basin would have caused significant crustal displacement and subsequent isostatic adjustment. Gravity data analysis can help evaluate the isostatic response to such an impact event. If the gravity data indicates isostatic compensation or flexure patterns consistent with a large impact and subsequent crustal adjustment, it provides support to accept the single impact hypothesis.

A feature that can help with accepting or rejecting both of these hypotheses, is the crater count or distribution of gravity anomalies. If gravity data can provide prove for multiple (subsurface) large impacts, it would favor the several large impact hypothesis. Also, if the crustal thickness variations on Mars are can be attributed to several impacts and is not only visible in a distinction between the northern and southern hemisphere, this rejects the single impact hypothesis. Gravity data can help identify additional impact structures by detecting gravity anomalies associated with these features. If the gravity data reveals multiple distinct gravity lows or anomalies corresponding to known impact basins, it would support the several impacts hypothesis. However, if the gravity data does not exhibit significant gravity anomalies beyond the Borealis Basin, it would suggest a stronger case for the single impact hypothesis.

It has, however, already been discussed by [Zuber et al., 2000] that the global distribution of the crustal thickness does not correlate with the dichotomy boundary. This does not mean that this never was the case. It might be that this distinction was there previously, but has been erased by subsequent processes. [Zuber et al., 2000] also discusses that the gravity anomaly does not correspond to a single or multiple large impact theory, as an early basin that remains unfilled would typically undergo compensation, while a filled basin, which aligns with the age of the northern surface, would likely exhibit a positive mass anomaly. This is not seen for the northern lowlands as a whole, although it is present in some places like the Utopia basin.

While gravity data can provide valuable insights, it is important to note that the presence of gravity anomalies consistent with, e.g., a single impact event does not conclusively prove the hypothesis. Distinguishing between all four hypotheses relies on an analysis that integrates gravity data with other geological, topographic, and geophysical studies. Therefore, it is not expected that this research will be able to determine which of the four hypotheses can be accepted. This research will, however, make use of gravity data and subsurface structures to find helpful evidence for potentially accepting or rejecting (one of) the hypotheses.

1.2. Martian interior

The core of Mars is supposed to be differentiated into two layers: a solid inner and molten outer core, however it is unclear what the density would be [Smrekar et al., 2019]. The radius of the core would be around 1800 km. Above this core, a liquid mantle is present. This mantle consists mostly of silicates. Recent studies, e.g. Broquet and Andrews-Hanna [2022], show that a big mantle plume underneath the Elysium rise is present. Gravity anomalies and volcanic activity in this area support the hypothesis of a mantle plume. This mantle plume was also studied at the TU Delft, in van der Tang [2021].

The knowledge of the Martian interior has increased greatly after the InSight mission. InSight landed on Mars in November 2018 and provides seismological data in the area of its landing site: Elysium Planitia. This data gives more information than the secondary gravity data that is retrieved from missions like Mars Global Surveyor (MGS) and Mars Reconnaissance orbiter (MRO). However, it only provides data at the landing site, making it not straightforwared to extrapolate this data to the rest of the planet. In the next two paragraphs, the main findings pre and post the InSight mission are presented.

The crustal thickness ranges are fairly insensitive to the structure and characteristics of the mantle and core [Wieczorek et al., 2022]. However, the uncertainty with using seismic constraints when determining the crustal thickness is fairly big as the amount of data points (marsquakes) is not high [Wieczorek et al., 2022].

Pre InSight

Wieczorek and Zuber [2004] found that the crust of the southern highlands is about 53 to 68 km thick, with an assumed crustal density of 2700 and 3100 kg/m^3, respectively. Within the uncertainty of 1σ that Wieczorek and Zuber [2004] define, the average crustal thickness ranges from 39 to 81 km. Neumann et al. [2004] created a global crustal thickness map,with a best fitting average crustal thickness of 45 km. McGovern [2004] used a regional isostasy method and found a crustal thickness range of 8 to 68 km, with a best fitting thickness of 50 km. Then, the density of the volcanic loads are determined to be close to 3200 kg/m^3, as, amongst others, defined by McGovern [2004] and Belleguic et al. [2005]. This seems to be consistent with the density of basaltic meteorites examined on Mars [Neumann et al., 2004]. In Belleguic et al. [2005] it is also found that the entire northern lowlands may be mostly composed of basalts. This is based on the finding that the density of the crust beneath the Elysium rise is the same as that of the volcanic load itself.

In Pauer and Breuer [2008] a maximum crustal density of 3020 kg/m^3 was assumed, finding a mean crustal thickness of 110 km. Baratoux et al. [2014] also shows that the mean crustal thickness could be around 110 km using a high crustal density of 3300 kg/m^3, based on the composition of the surface. These crustal density estimates are mean values of the crust densities that most likely vary around the whole surface of Mars.

To obtain properties of the lithosphere, a common approach is to relate this to the effective elastic lithosphere thickness, This describes the manner in which the lithosphere responds to a certain loading. In Zuber et al. [2000], the elastic thickness of Mars is divided into three main regions: 0 to 20 km in the southern highlands, about 50 km in the Alba Patera region and an even larger elastic thickness of about 100 km in the Tharsis region. In Smrekar et al. [2019], it is also discussed that research shows that higher elastic thickness is related to being a younger surface. E.g. Phillips et al. [2008] showed that present-day elastic thickness values can be even larger than 300 km.

Post InSight

In Knapmeyer-Endrun et al. [2021], the seismometer on board of Insight was used to determine the thickness of the Martian crust. Based on two different models, the thickness of the crust at the landing site is 15 to 47 km. This is thinner than previously expected [Wieczorek and Zuber, 2004]. Knapmeyer-Endrun et al. [2021] also extrapolated this data to a global mean crustal thickness, where the two different models gave crustal thicknesses between 24 to 72 km. They used a maximum density of 2850 kg/m^3. This is supported by the findings of Kim et al. [2023], who finds that the mean crustal thickness is 42-56 km. The crust at Elysium Planitia is thus thinner than the global mean crustal thickness. Another research, Liang et al. [2022], finds that the crustal density beneath Elysium should be around 3000 kg/m^3.

The lithospheric thickness has also been constrained a bit more using InSight. In Khan et al. [2021], it is mentioned again that the crust-mantle interface lies around 30 to 50 km. In this paper, models using lithospheric thicknesses of 400-500 km and 500-600 km are used. The inversion of the S- and P waves together with heat flow agree with this. Zhong et al. [2022] studied the elastic lithospheric thickness at Olympus and Elysium, and found values of 88 km and 28 km, respectively. They applied the same method to Isidis basin, and found that an elastic thickness between 55 and 110 km. This corresponds to a crustal density of 2665 kg/m^3 and 2900 kg/m^3, respectively. They discuss that the small elastic thickness at Isidis Planitia is more likely, due to the origin of Isidis Planitia and the volcanism that happened after. Ding et al. [2019] found elastic lithospheric thicknesses of 210 km at some locations on Mars. Other studies, like McGovern [2004] and [Ritzer and Hauck, 2009], find values in between the range of 28 km to 210 km.

1.3. Gravity and spherical harmonics

In order to use and interpret gravity data of Mars, it is important to first understand the basics of gravity. Modelling gravity on a spherical surface can be done using spherical harmonics.

A short introduction on gravity and the spherical harmonic representation of gravity is presented in this section. All information is obtained from the following sources: [Ermakov et al., 2018], [Watts and Moore, 2017], [Kaula, 1963], [Schrama, 2020], [Root, 2021], [Wieczorek and Simons, 2005] and [Neumann et al., 2004].

All masses attract each other with a gravitational force that can be described as

$$F = -G\frac{m_1 m_2}{d^2} \tag{1.1}$$

in which F is the force in Newton, G the gravitational constant ($6.67 \cdot 10^{-11}$ m^3/kg/s^2), m_1 and m_2 the masses of the two bodies in kilogram and d the distance between the two bodies in meter. Then, according to Newton's second law, the acceleration of the first body is

$$a_1 = \frac{F_1}{m_1} = -\frac{Gm_2}{d^2}. \tag{1.2}$$

Therefore, the acceleration of the body is independent of its own mass. From this, the gravitational field $\vec{g}(\vec{r})$ can be defined as

$$\vec{g}(\vec{r}) = -GM\frac{\vec{r}}{|\vec{r}|^3} \tag{1.3}$$

in which M is now the mass of the attracting (spherically symmetric) body and $\vec{r}$ the vector describing the distance to the measuring point.

This can, in fact, be related to the gravitational potential V as follows

$$\vec{g}(\vec{r}) = -\nabla V(\vec{r}), \tag{1.4}$$

giving

$$V(\vec{r}) = \frac{GM}{|\vec{r}|}, \tag{1.5}$$

where $\vec{r}$ is still the distance to the attracting body.

In order to represent this gravitational data in such a way that it can be interpreted, visualized and analyzed on a spherical surface, the gravity models of Mars use a spherical harmonic representation. Real spherical harmonics can be described as

$$Y_{nm}(\theta, \phi) = \begin{cases} \bar{P}_{nm}(\cos\theta)\cos m\phi & \text{if } m \geq 0 \\ \bar{P}_{n|m|}(\cos\theta)\sin|m|\phi & \text{if } m < 0 \end{cases}, \tag{1.6}$$

where $\bar{P}_{nm}$ are the normalized associated Legendre functions of the degree n and order m. θ and ϕ describe the planetocentric co-latitude and longitude respectively. $\bar{P}_{nm}$ can then be described as a function of the unnormalized Legendre functions P_{nm} as follows

$$\bar{P}_{nm}(\mu) = \sqrt{(2-\delta_{0m})(2n+1)\frac{(n-m)!}{(n+m)!}}P_{nm}(\mu). \tag{1.7}$$

In this equation, δ_{0m} is the Kronecker delta function.The unnormalized Legendre functions P_{nm} are related to the Legendre polynomials as described in

$$P_{nm}(\mu) = \left(1-\mu^2\right)^{m/2} \frac{\mathrm{d}^m}{\mathrm{d}\mu^m} P_n(\mu) P_n(\mu) = \frac{1}{2^n n!} \frac{\mathrm{d}^n}{\mathrm{d}\mu^n} \left(\mu^2 - 1\right)^n . \tag{1.8}$$

Using Equation 1.6, the potential V exterior to mass M, can be expressed as a function of spherical harmonic functions. The part from Equation 1.5 that is rewritten to spherical harmonics is the $\frac{1}{||\vec{r}||}$ term, as presented in Root et al. [2016]. This gives

$$V(\vec{r}) = \frac{GM}{r} \sum_{n=0}^{\infty} \sum_{m=-n}^{l} \left(\frac{R_0}{r}\right)^n C_{nm} Y_{nm}(\theta, \phi). \tag{1.9}$$

In this equation, R_0 describes the reference radius of the body considered. Also, C_{nm} describes the Stokes coefficients with degree n and order m. The Stokes coefficients represent the spherical harmonic coefficients at R_0 and are thus a subset of the spherical harmonic coefficients. Then, taking the derivative of Equation 1.9, with respect to r, gives back the radial gravitational potential. This time expressed as functions of spherical harmonics:

$$g_r = -\frac{GM}{r^2} \sum_{n=0}^{\infty} \sum_{m=-n}^{n} \left(\frac{R_0}{r}\right)^n (n+1) C_{nm} Y_{nm}(\theta, \phi). \tag{1.10}$$

Taking again the derivative with respect to r, the gravitational tensor can be derived as follows:

$$T_{rr} = \frac{GM}{r^3} \sum_{n=0}^{\infty} \sum_{m=-n}^{n} \left(\frac{R_0}{r}\right)^n (n+2)(n+1) C_{nm} Y_{nm}(\theta, \phi) \tag{1.11}$$

In the last two equations, g_r and T_{rr} are both defined as positive downwards.

It must be noted that the spherical harmonic degree n is related to an equivalent wavelength λ as follows:

$$\lambda = \frac{2\pi R}{\sqrt{n(n+1)}} \tag{1.12}$$

where R is the radius of the sphere considered [Wieczorek and Simons, 2005]. This is a way to describe a certain degree n in a distance unit (wavelength) and therefore couple a degree to a geophysical feature.

Some spherical harmonic coefficients have specific physical interpretations. C_{00} describes the mass of the planet itself, while degree 1 terms are related to the shift of the center of mass and degree 2 terms are related to the moment of inertia of the body. For example, C_{20} describes the flattening of the planet [Schrama, 2020] [Watts and Moore, 2017].

1.4. Research aim and research question

From section 1.1, it is clear that gravity data research can provide valuable insights on the geology and geological history of Mars. Two typical methods to use gravity data are forward modelling or inversion. These are opposite to each other. Forward modelling uses a known model and known input parameters to compute the gravity anomalies, such that these can be compared to the actual gravity observations. Gravity inversion uses a known model and the observed gravity anomalies, to compute the input parameters that best fit this inversion. In this case, the input parameters (e.g. crustal density) of the interior model are not yet known. Therefore, gravity inversion will be used. By modelling crustal and lithospheric mass density features, one can determine the effect of these features on gravity anomalies. Then, more can be said about the internal structure of Mars.

Inversion methods have been used in previous gravity research. In these studies, assumptions on the Martian interior have been made. An important assumption is the isostasy mode of the mantle supporting the crust. From multiple studies (e.g. [Mussini, 2020], [Sleep and Phillips, 1985]) it becomes clear the Mars is dominated by flexural isostasy, however there might also be local isostasy present at locations like Tharsis. In Qin [2021], for example, it becomes clear that the elastic lithospheric thickness is around 160 km, while other studies find values of 28 km [Zhong et al., 2022] to 210 km [Ding et al., 2019]. These discrepancies between papers also occur for the crustal thickness and densities. Qin [2021] showed that flexural isostasy can provide the best estimates for Mars, with assuming a homogeneous crustal density. However, in reality the Martian crust and lithosphere do not have a homogeneous density. Therefore, van Brummen [2022] researched lateral density variations using gravity inversion. This inversion only included the isotropic kernel in the vertical-vertical direction, K_{rr}. It seems therefore likely that the inclusion of the isotropic kernels $K_{r\Omega}$ and $K_{\Omega\Omega}$ will improve the gravity inversion method. Also, van Brummen [2022] assumes that all columns have an equal mass. Next to this assumption, most research assumes either a homogeneous crustal density, or homogeneous crustal thickness. This research will vary both, such that the interior model becomes more realistic.

Next to geological assumptions, the inversion algorithm also needs input parameters to be determined. These input parameters, like the weights used in the least-squares solution, can be tested using a synthetic planet. Previous research did limited research on this, or assumed values based on other previous research. In this research, a more extensive sensitivity analysis using the input parameters will be performed, such that the inversion can be executed using the correct input parameters. Chapter 2 elaborates on these input parameters and the sensitivity analysis.

Concluding this section, the aim of of this study is to define new inversion methods that allow for a further understanding of the Martian crustal and mantle densities. These new inversion methods are defined in Chapter 2. The research question that accompanies this aim is:

How can subsurface density variations be obtained by a two-layer gravity inversion, in order to better understand Martian surface features and their geological history?

1.5. Report outline

After defining the research aim and presenting the background information leading to this objective, the rest of this thesis report can be introduced. First, chapter 2 introduces the basics of an inversion. It does so by first introducing the least-squares algorithm that is used. Then, the implementation of this least-squares problem into the Martian gravity field is explained. Finally, a preliminary study on the analysis of several input parameters of the inversion is shown in section 2.3. This preliminary study is used as a basis for the two-layer inversion.

The two-layer inversion is presented in the form of a journal article. This journal article is included in this report in chapter 3. This article contains the methodology, results, conclusions and a discussion of this research.

Afterwards, chapter 4 presents the verification and validation of the data sets that are used in this research: MOLA and MRO120F. Also, it presents information about specific Matlab tools that are used for this research. Then, small analyses on the data are performed using these Matlab tools, in order to better validate the use case of the tools for this project. This is presented in section 4.2 and section 4.3. This chapter is concluded with a short validation of the one-layer inversion.

The final conclusions and recommendations are presented in chapter 5. This chapter supplements the conclusions that are already drawn in chapter 3.

2

Preliminary study: One-layer inversion

In the final research as presented in Chapter 3 a two-layer inversion will be performed. In order to create this two-layer inversion, first a one-layer inversion was studied as preliminary work. This process is elaborated upon in this chapter. Inversions are commonly performed using a least-squares method. Therefore, section 2.1 will first elaborate on which least-squares algorithm is used. Then, section 2.2 shows how the least-squares algorithm can be implemented in the one-layer gravity inversion. Finally, the preliminary study on the one-layer inversion is presented in section 2.3. It also describes which conclusions can be drawn from this study.

2.1. An introduction to the least-squares problem

The general form of a linear least-squares problem is

$$\bar{y} = A\bar{x} + \bar{\epsilon}. \tag{2.1}$$

In this equation, the matrix $\bar{y}$ contains the observations. A is the design matrix containing the model equations and $\bar{x}$ represents all the input parameters. $\bar{\epsilon}$ is the error between the model and the observations. The aim of this problem is to minimise the error $\bar{\epsilon}$. In order to minimize this, the cost function

$$J = \bar{\epsilon}^t P_{yy}^{-1} \bar{\epsilon} \tag{2.2}$$

is introduced. In cost function J, the covariance matrix P_{yy} is appearing. This matrix describes the correlation between or noise within the observations. If the observations correlate to each other, the diagonal will contain the variance of these observations and the rest of the values will be zero. Rewriting Equation 2.1 and substituting it in Equation 2.2, gives the following:

$$J = \bar{y}^t P_{yy}^{-1}(\bar{y} - A\bar{x}) - \bar{x}^t A^t P_{yy}^{-1}(\bar{y} - A\bar{x}). \tag{2.3}$$

Using the covariance matrix makes the least-squares problem a so-called weighted least-squares problem. The minimum of J should be obtained using Equation 2.3. The first term can not be minimized, as, when $\bar{y} - A\bar{x} \approx 0$, the term will not have any effect. Therefore, $\bar{x}^t A^t P_{yy}^{-1}(\bar{y} - A\bar{x})$ should be minimized. Then, excluding the trivial solution that $\bar{x} = 0$, the following equation presents itself:

$$\hat{x}^t A^t P_{yy}^{-1}(\bar{y} - A\hat{x}) = 0. \tag{2.4}$$

The hat on matrix x shows that this is the solution of the weighted least squares problem. Rewriting it to isolate $\hat{x}$ gives

$$\hat{x} = \left(A^t P_{yy}^{-1} A\right)^{-1} A^t P_{yy}^{-1} \bar{y} = B\bar{y}. \tag{2.5}$$

Solving this, will lead to a solution of the weighted least squares problem $\bar{y} = A\bar{x} + \bar{\epsilon}$. The solution, however, will also have a covariance matrix. This parameter covariance matrix is denoted by P_{xx}. As the problem considered is a linear problem, it is possible to obtain P_{xx} simply by applying a linear transformation on P_{yy}.

$$P_{xx} = BB^t \tag{2.6}$$

With writing out B (as derived in Equation 2.5) and applying matrix simplifications, the final equation for P_{xx} can be obtained:

$$P_{xx} = \left(A^t P_{yy}^{-1} A\right)^{-1} A^t P_{yy}^{-1} P_{yy}^{-1} P_{yy} A \left(A^t P_{yy}^{-1} A\right)^{-1} = \left(A^t P_{yy}^{-1} A\right)^{-1}. \tag{2.7}$$

As becomes clear from Equation 2.7, the parameter covariance matrix is directly related to the observation variance matrix.

If the independent variable of the least-squares problem are highly correlated, the matrix $A^t P_{yy}^1 A$ can become near-singular. This will induce higher variances in the parameter covariance matrix P_{xx}. Therefore, a ridge regression, or Tikhonov regularization, can be introduced. The ridge regression is based on adding a diagonal matrix defined as λI to the moment matrix $A^t P_{yy}^1 A$. λ is then the ridge parameter and I is an identity matrix. Adding this ridge regression leads to the following new least-squares solution:

$$\hat{x} = \left(A^t P_{yy}^{-1} A + \lambda I\right)^{-1} A^t P_{yy}^{-1} \bar{y}. \tag{2.8}$$

As determining the value of λ might seem arbitrary, a method for this can be used. This method makes use of the so-called L-curve. An example of such a curve is presented in Figure 2.1 [Hansen, 2001]. On the horizontal axis, the residual norm of the solution is plotted, while on the vertical axis the norm of the solution is plotted. The residual norm is presented as $||Ax_\lambda - b_\lambda||$, with b being the observation data matrix - the equivalent of y in this chapter. Different values for λ gives a different ratio between the solution norm and the residual norm. The name of the L-curve originates from its shape. The 'corner' of the L is the point with the optimal value of λ. On the left side of this turn-around point, the residual norm only decreases insignificantly, while the solution norm blows up. This means that one is 'over fitting' the least-squares problem. On the right-hand side of the turn-around point, the residual norm starts to increase very significantly, without reducing the solution norm anymore. This means that one is 'under fitting'/smoothing out the solution too much. The corner of the L-curve is the value of λ that gives the best ratio between the solution norm and the residual norm. In the case of the L-curve in Figure 2.1, $\lambda = 0.01$ would give the best solution. Per least-squares problem, the value for λ might be different.

The principle of this L-curve was used to design our own experiment to find the most optimal value for λ. This experiment is performed in combination with the values for σ (weights of the observations) and the height of the observations. This analysis is presented in section 2.3.

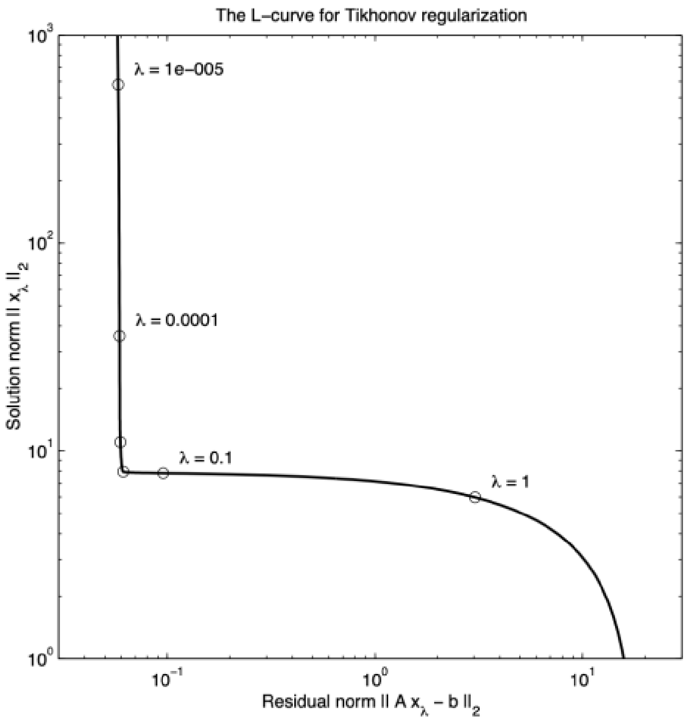

Figure 2.1: An example of an L-curve for a standard ridge regression, where $x_0 = 0$ [Hansen, 2001].

2.2. Implementation of the one-layer gravity inversion

Gravity gradients represent the derivative of gravity in the spatial domain, in three directions: radial, lateral and axial. In spherical coordinates this is denoted with (r, θ, ϕ). The gravity gradient in the radial direction can be denoted as Γ_{rr}, describing the derivative of the radial component of the gravity g_r w.r.t r. The gravity gradients are present in all directions: Γ_{rr}, $\Gamma_{\theta\theta}$, $\Gamma_{\phi\phi}$ and also $\Gamma_{r\theta}$, $\Gamma_{r\phi}$ and $\Gamma_{\theta\phi}$. In fact, these gravitational gradient tensor $\mathbf{\Gamma}$ is the double gradient of the gravitational potential V, as described in section 1.3.

$$\mathbf{G} = \text{gradgrad}V \tag{2.9}$$

In order to derive which topographic feature attributes to the gravity gradients, it is important to compute the distance between the measurement point and the topographic feature considered. This can be done by the Green's function $G(r, r')$, which is defined as

$$G(\bar{r}, \bar{r}') = \frac{1}{L(\bar{r}, \bar{r}')}. \tag{2.10}$$

In this equation, L represents the distance between the points $\bar{r}$ and $\bar{r}'$ and is given as

$$L(r, \psi, r') = \sqrt{r^2 + r'^2 - rr'cos\psi}, \tag{2.11}$$

with r and r' being the magnitudes of vectors $\bar{r}$ and $\bar{r}'$, respectively. Also, ψ is the angular distance between the directions of the two vectors $\bar{r}$ and $\bar{r}'$. Using Equation 2.9, Equation 2.10 and Equation 2.11, Martinec [2014] derived the Green's function in spherical coordinates (r, θ, ϕ) as seen in

$$\begin{aligned}\text{gradgrad}\,\frac{1}{L} =& \frac{1}{r^3}\Big[K_{rr}(t,x)\boldsymbol{e}_{rr} + 2K_{r\Omega}(t,x)\left(\cos\alpha\boldsymbol{e}_{r\vartheta} - \sin\alpha\boldsymbol{e}_{r\varphi}\right)\\ &+K_{\Omega\Omega}(t,x)\left(\cos 2\alpha\left(\boldsymbol{e}_{\vartheta\vartheta} - \boldsymbol{e}_{\varphi\varphi}\right) - 2\sin 2\alpha\boldsymbol{e}_{\vartheta\varphi}\right) - \frac{1}{2}K_{rr}(t,x)\left(\boldsymbol{e}_{\vartheta\vartheta} + \boldsymbol{e}_{\varphi\varphi}\right)\Big].\end{aligned} \tag{2.12}$$

In Equation 2.12, α is the azimuthal angle and Ω denotes both the co-latitude θ as well as the longitude ϕ, such that $K_{r\Omega} = K_{r\theta} = K_{r\phi}$. K_{rr}, $K_{r\Omega}$ and $K_{\Omega\Omega}$ are the isotropic kernels, describing the influence of the topographic feature on the measurement point in the three directions. In these kernels, $t = \frac{r'}{r}$ and $x = \cos\psi$. The vectors $\mathbf{e}$ are unit vectors in the respective directions. The isotropic kernels can be defined by Legendre polynomials and their derivatives. This is also presented by Martinec [2014].

$$\begin{aligned}K_{rr}(t,x) &= \sum_{j=0}^{\infty}(j+1)(j+2)t^j P_j(x)\\ K_{r\Omega}(t,x) &= -\sqrt{1-x^2}\sum_{j=0}^{\infty}(j+2)t^j\frac{dP_j(x)}{dx}\\ K_{\Omega\Omega}(t,x) &= \frac{1}{2}\left(1-x^2\right)\sum_{j=0}^{\infty}t^j\frac{d^2P_j(x)}{dx^2}\end{aligned} \tag{2.13}$$

Now, this should be written in a closed form, which is also presented by Martinec [2014]. They showed that

$$K_{rr}(t,x) = -\frac{1}{g^3} + \frac{3(1-tx)^2}{g^5}, \tag{2.14}$$

$$K_{r\Omega}(t,x) - = \sqrt{1-x^2}\frac{3t(1-tx)}{g^5}, \tag{2.15}$$

$$K_{\Omega\Omega}(t,x) = \frac{1}{2}\sqrt{1-x^2}\frac{3t^2}{g^5}, \tag{2.16}$$

with $g = \sqrt{1+t^2-2tx}$. With these closed form isotropic kernels, it is possible to compute the mass distribution w.r.t. the computation point. In Figure 2.2 the behaviour of the three kernels is visible. It shows that the vertical-vertical kernel (K_{rr}) has the most impact when the topographic feature is right beneath the computation point, and the further away (with ψ) the mass occurs the less influence it has on the vertical-vertical gradient. For the vertical-horizontal kernel ($K_{r\Omega}$) this is not the case. Here, the densities with a small, but non-zero, angular degree have a greater impact than for $\psi = 0$ or larger values of ψ. This is also the case for the horizontal-horizontal kernel ($K_{\Omega\Omega}$), for which the peak is smoothed out (w.r.t. the curve of $K_{r\Omega}$). One can expect that the closer the measurement point is to the observed mass, the more impact all kernels will have. Especially, the K_{rr} kernels becomes relatively strong [Martinec, 2014]. The behaviour and impact of the different kernels also changes with the height of the computation point.

Using these kernels, it is possible to derive the design matrix A and the input parameters of the least-squares problem as described in section 2.1. To do this, first the gravitational gradient tensor is shown in

$$\mathbf{\Gamma} = \mathbf{\Gamma}_{rr} + \mathbf{\Gamma}_{r\Omega} + \mathbf{\Gamma}_{\Omega\Omega}. \tag{2.17}$$

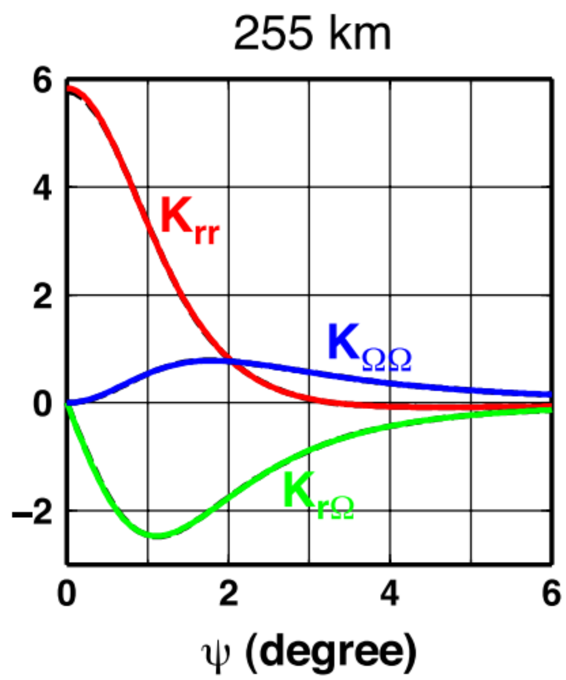

Figure 2.2: This figure, obtained from Martinec [2014], shows the isotropic kernels K_{rr}, $K_{r\Omega}$ and $K_{\Omega\Omega}$ as a function of the angular distance ψ and at a height of the computation point of 255 km. For this figure the radius of the Earth is used.

The gravitational gradient tensor can be related back to Equation 1.5, such that

$$\mathbf{\Gamma}(\vec{r}) = G \int_v \varrho(\vec{r}')\boldsymbol{G}(\vec{r}, \vec{r}')dV. \tag{2.18}$$

In this, G is the gravitational constant just like in section 1.3. $\boldsymbol{G}(\vec{r}, \vec{r}')$ is the Greens' function as also described in Equation 2.10. Finally, $\varrho(\vec{r}')dV = \mathrm{d}m$ is the mass element considered. The gravitational gradient tensor $\mathbf{\Gamma}$ then also consists of the three components in different directions. These three components can be expressed using the following expressions, given by Martinec [2014]:

$$\mathbf{\Gamma}_{rr} = D_{rr}\left[\boldsymbol{e}_{rr} - \frac{1}{2}\left(\boldsymbol{e}_{\vartheta\vartheta} + \boldsymbol{e}_{\varphi\varphi}\right)\right], \tag{2.19}$$

$$\mathbf{\Gamma}_{r\Omega} = 2D_{r\vartheta}\boldsymbol{e}_{r\vartheta} - 2D_{r\varphi}\boldsymbol{e}_{r\varphi}, \tag{2.20}$$

$$\mathbf{\Gamma}_{\Omega\Omega} = D_{\vartheta\vartheta\varphi\varphi}\left(\boldsymbol{e}_{\vartheta\vartheta} - \boldsymbol{e}_{\varphi\varphi}\right) - 2D_{\vartheta\varphi}\boldsymbol{e}_{\vartheta\varphi}. \tag{2.21}$$

In these three expressions, use is made of the five radially dependent functions D_{rr}, $D_{r\theta}$, $D_{r\phi}$, $D_{\theta\theta\phi\phi}$, $D_{\theta\phi}$, which again depend on the isotropic kernels as described in Equation 2.13.

$$D_{rr}(r) = \frac{G}{r^3}\int_V \varrho(\vec{r}')K_{rr}(t, \cos\psi)dV, \tag{2.22}$$

$$\left\{\begin{array}{c} D_{r\vartheta}(r) \\ D_{r\varphi}(r) \end{array}\right\} = \frac{G}{r^3}\int_V \varrho\left(\vec{r}'\right)K_{r\Omega}(t, \cos\psi)\left\{\begin{array}{c} \cos\alpha \\ \sin\alpha \end{array}\right\}dV, \tag{2.23}$$

$$\left\{\begin{array}{c} D_{\vartheta\vartheta\varphi\varphi}(r) \\ D_{\vartheta\varphi}(r) \end{array}\right\} = \frac{G}{r^3}\int_{\mathcal{V}} \varrho\left(\vec{r}'\right)K_{\Omega\Omega}(t, \cos\psi)\left\{\begin{array}{c} \cos 2\alpha \\ \sin 2\alpha \end{array}\right\}dV. \tag{2.24}$$

In these radially dependent functions, it must be noted again that $\varrho(\vec{r}')$ is the mass density function, dependent on the radial position, that ψ represents the spherical distance between the computation point and the mass element dm and α represented the azimuthal distance between these two points. From these functions, the input for the design matrix A can be determined. If one determines the mass element of interest, and one assumes a constant density within the mass element i, the gravitational gradient tensor in the vertical-vertical direction can be expressed as

$$\mathbf{\Gamma}_{rr} = \frac{G}{r^3}\rho_i K_{rr,i} V_i, \tag{2.25}$$

with ρ_i and V_i being the density and volume of the mass element of interest, respectively. Now, this needs to be related back to the linear least-squares problem $\hat{x} = \left(A^t P_{yy}^{-1} A + \lambda I\right)^{-1} A^t P_{yy}^{-1} \bar{y}$. As the volume of the mass element considered is known, ρ is the unknown parameter that needs to be solved for, so $\bar{x}_{rr} = \rho$. Then, the design matrix can be defined as $A_{rr} = \frac{G}{r^3} K_{rr} V$, with r being the distance between the mass and the computation point. Now, A and $\bar{x}$ also need to be determined for the isotropic kernels in other directions. This can be done in the same way as for Γ_{rr}, giving the following radial functions.

$$\mathbf{\Gamma}_{r\theta} = 2\frac{G}{r^3}\rho K_{r\Omega}\cos(\alpha)V, \tag{2.26}$$

$$\mathbf{\Gamma}_{r\phi} = -2\frac{G}{r^3}\rho K_{r\Omega}\sin(\alpha)V, \tag{2.27}$$

$$\mathbf{\Gamma}_{\theta\theta\phi\phi} = \frac{G}{r^3}\rho K_{\Omega\Omega}\cos(2\alpha)V, \tag{2.28}$$

$$\mathbf{\Gamma}_{\theta\phi} = -2\frac{G}{r^3}\rho K_{\Omega\Omega}\sin(2\alpha)V. \tag{2.29}$$

From this, the design matrices are constructed as follows:

$$A_{rr} = \frac{G}{r^3} K_{rr} V, \tag{2.30}$$

$$A_{r\theta} = 2\frac{G}{r^3} K_{r\Omega}\cos(\alpha)V, \tag{2.31}$$

$$A_{r\phi} = -2\frac{G}{r^3} K_{r\Omega}\sin(\alpha)V, \tag{2.32}$$

$$A_{\theta\theta} = \frac{G}{r^3} K_{\Omega\Omega}\cos(2\alpha)V, \tag{2.33}$$

$$A_{\phi\phi} = \frac{G}{r^3} K_{\Omega\Omega}\cos(2\alpha)V, \tag{2.34}$$

$$A_{\theta\phi} = -2\frac{G}{r^3} K_{\Omega\Omega}\sin(2\alpha)V. \tag{2.35}$$

Now that the different components of the design matrix A are determined, a step back should be taken. The different parts of the least-squares equation $\bar{y} = A\bar{x}$ can now be fully defined. The amount of observations are denoted using subscript i, where 1 is the first observation point and I the last. Then, the observation matrix $\bar{y}$ is defined as

$$\bar{y} = \begin{bmatrix} \Gamma rr, 1 \\ \vdots \\ \Gamma_{rr,I} \\ \Gamma_{r\theta,1} \\ \vdots \\ \Gamma_{r\theta,I} \\ \Gamma_{r\phi,1} \\ \vdots \\ \Gamma_{r\phi,I} \\ \Gamma_{\theta\theta,1} \\ \vdots \\ \Gamma_{\theta\theta,I} \\ \Gamma_{\phi\theta,1} \\ \vdots \\ \Gamma_{\phi\theta,I} \\ \Gamma_{\theta\theta,1} \\ \vdots \\ \Gamma_{\theta\theta,I} \end{bmatrix}, \tag{2.36}$$

such that is has the shape $(6i, 1)$. Now, output matrix $\bar{x}$ is defined as

$$\bar{x} = \begin{bmatrix} \rho_1 \\ \vdots \\ \rho_I \end{bmatrix}, \tag{2.37}$$

thus having a shape of $(i, 1)$. Finally, the design matrix A is constructed as follows:

$$A = \frac{G}{r^3} \begin{bmatrix} K_{rr,1}V_1 & \dots & K_{rr,1}V_I \\ \vdots & & \vdots \\ K_{rr,I}V_1 & \dots & K_{rr,I}V_I \\ -\frac{1}{2}K_{rr,1}V_1 & \dots & -\frac{1}{2}K_{rr,1}V_I \\ \vdots & & \vdots \\ -\frac{1}{2}K_{rr,I}V_1 & \dots & -\frac{1}{2}K_{rr,I}V_I \\ 2\cos\alpha K_{r\Omega,1}V_1 & \dots & 2\cos\alpha K_{r\Omega,1}V_I \\ \vdots & & \vdots \\ 2\cos\alpha K_{r\Omega,I}V_1 & \dots & 2\cos\alpha K_{r\Omega,I}V_I \\ -2\sin\alpha K_{r\Omega,1}V_1 & \dots & -2\sin\alpha K_{r\Omega,1}V_I \\ \vdots & & \vdots \\ -2\sin\alpha K_{r\Omega,I}V_1 & \dots & -2\sin\alpha K_{r\Omega,I}V_I \\ -2\sin 2\alpha K_{\Omega\Omega,1}V_1 & \dots & -2\sin 2\alpha K_{\Omega\Omega,1}V_I \\ \vdots & & \vdots \\ -2\sin 2\alpha K_{\Omega\Omega,I}V_1 & \dots & -2\sin 2\alpha K_{\Omega\Omega,I}V_I \\ 2\cos 2\alpha K_{\Omega\Omega,1}V_1 & \dots & 2\cos 2\alpha K_{\Omega\Omega,1}V_I \\ \vdots & & \vdots \\ 2\cos 2\alpha K_{\Omega\Omega,I}V_1 & \dots & 2\cos 2\alpha K_{\Omega\Omega,I}V_I \end{bmatrix}, \tag{2.38}$$

ending up with a shape of $(6i, i)$. The factors that are used before all the kernels originate from Equation 2.19 - Equation 2.21.

2.3. Sensitivity analysis on λ, σ and satellite height

In order to define a stable inversion, the input parameters of the least-squares problem need to be constrained. Specifically, the regularization parameter λ, the weights σ and the height of the observations need to be determined. The sensitive behaviour of λ was already presented in section 2.1. Therefore, a sensitivity analysis on these parameters is performed.

This is done using a two-layer model, using synthetic topography, synthetic crustal density and a synthetic mantle density pattern. This synthetic model is created using the Matèrn covariance function, as explained in van Brummen [2022]. The crust-mantle boundary is created using the topography and the flexure theory of Qin [2021]. This two-layer model is used for a one-layer inversion: only the crust or the mantle was inverted, using the 'known' values of the other layers density pattern as the gravity input of that layer. This allows for an analysis where the inversion only has one unknown: the density variations of the inverted layer. As the result of the inversion can be compared with the true density variations of the synthetic model, the arising errors can be attributed to the inversion itself.

Different two-layer models are created, using several combinations of layer thickness and layer depth. Also, every model is ran using the gravitational potential, vector and tensor. Then, all different interior model scenarios are performed with a series of values for σ, λ and height.

First, an analysis on λ and σ is performed. For all different scenario's (layer depths and thicknesses), it turned out that there is an optimal combination of of λ and σ yielding the lowest residual. Figure 2.3 shows a heatmap of the residuals after 6 iterations, using different values of λ and σ. The unit of the colorbar is $\mathrm{kg/m^3}$ and denotes the root-mean-square of the error density of the inverted layer. This shows a linear relationship between the optimal values for λ and σ.

Layers at different depths or with different thicknesses (within the range that makes sense) show the same results. Thus, it can be concluded that the depth and thickness of the layer does not impact the optimal combination of λ and σ. However, from the sensitivity analysis it became clear that the influence of gravity component used in the inversion is of severe importance. All the gravity components have a different sensitivity to the weights and regularization parameters. Figure 2.4 shows the optimal combination for each of the gravity components. These equations are set up using the heatmaps as shown in Figure 2.3.

Next to running the different values of λ and σ, also a qualitative analysis should be made, especially on what happens when this combination turns out not to be stable. When you are performing an inversion on Mars, you just have the outcome of the density patterns, but you do not know how it compares to the true density pattern. Therefore, it is of importance to know what happens in the inversion by only looking at the outcome of the density patterns. Figure 2.5 shows this, using the same heat map as in Figure 2.3. If the value of λ is too big for the weights, the input of the gravity observations does not get used in the inversion: the density residual is very large. On the other hand, when the regularization parameter gets too small compared to the weights, the noise of the observation data gets too much influence. This induces polar instabilities. The density is correctly inverted, but the poles experience too much instability. This is likely due to the amount of data points that are very close together at the poles.

Having these optimal λ-σ combinations, a closer look can be taken to the optimal satellite height of the observations. For a stable combination of λ and σ, the height was altered in the inversion. This yields to new graphs, of which one is shown in Figure 2.6. From this, it is clear that there exists an optimal height of the satellite observations for each combination of λ and

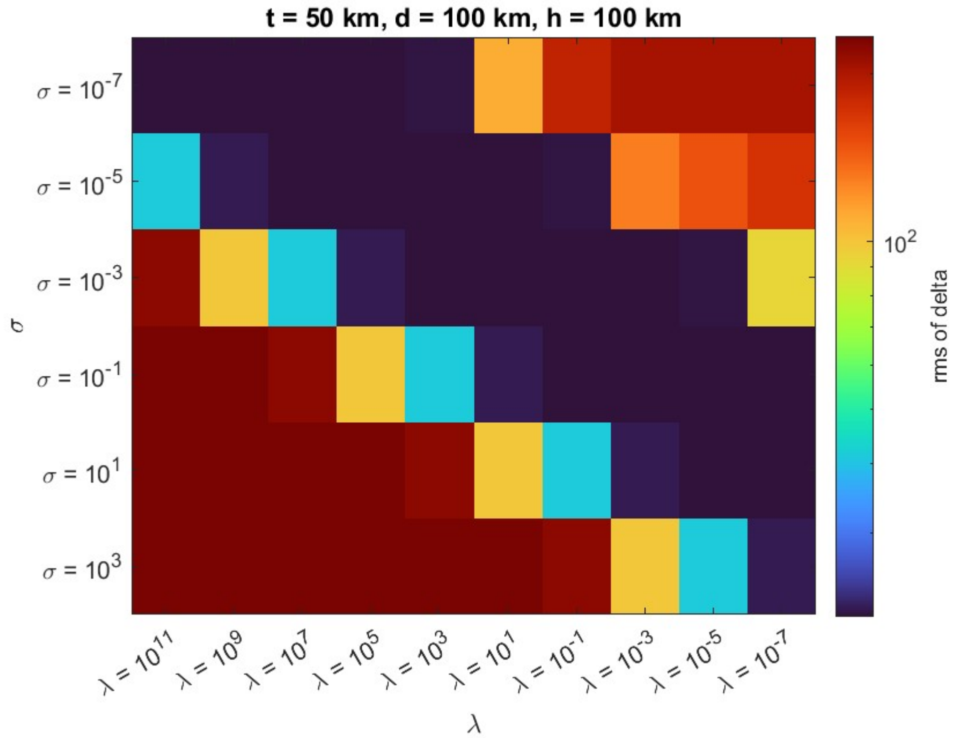

Figure 2.3: A sensitivity analysis of λ and σ on a model with a crust that has a depth of 100 km and a thickness of 100 km. The satellite height of the observations is 200 km. The inversion is performed using the gravitational potential.

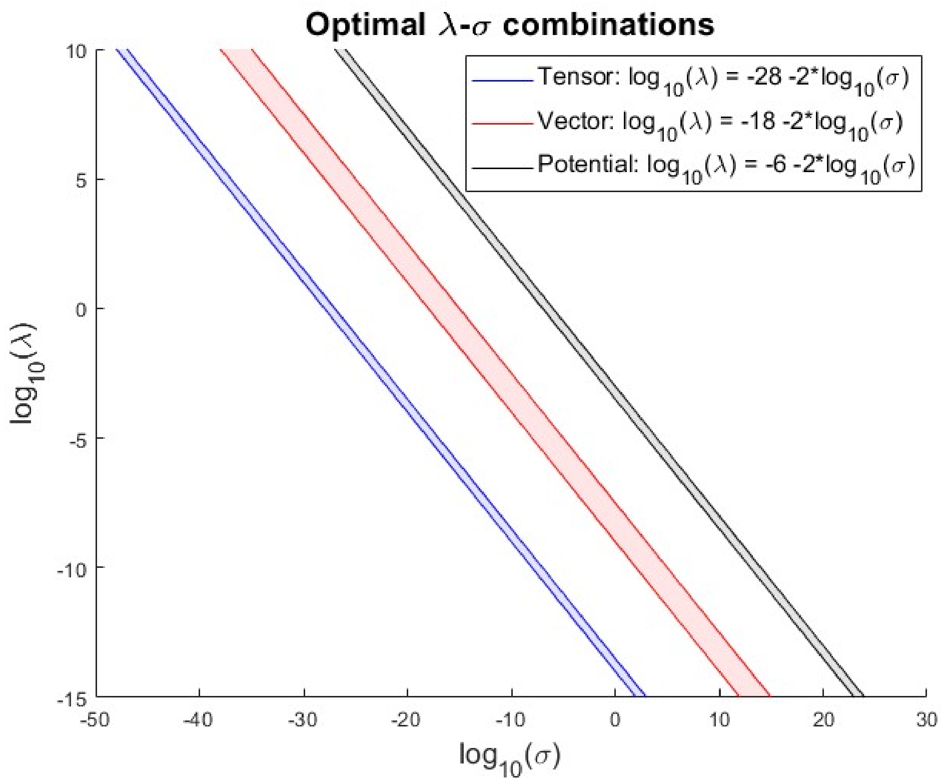

Figure 2.4: The optimal combinations for λ and σ to be used in the weighted, regularized, least-squares problem. Described for all three gravity components.

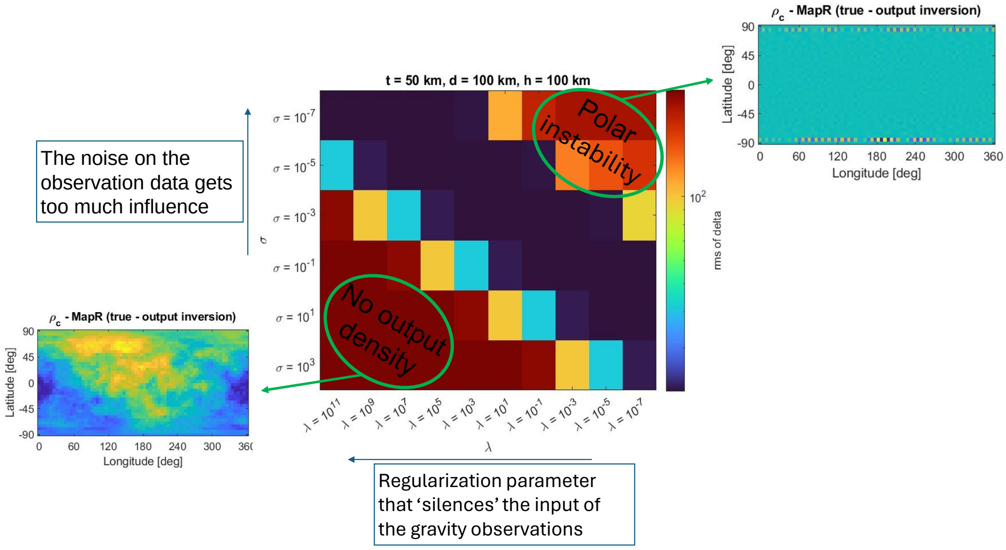

Figure 2.5: A qualitative analysis of the effect of a stable and unstable λ-σ combination

Table 2.1: Final input values for σ, λ and height of satellite observations to be used in the least-squares algorithm

Gravity component	σ	λ	Height [km]
Tensor	10^{-10}	10^{-7}	100
Vector	10^{-5}	10^{-5}	100
Potential	10^{-3}	10^{5}	100

σ. This optimal height is different for gravitational tensor, vector and potential, due to their different responses to height. As is shown in section 1.3, r is to the power 1, 2 and 3 respectively. Therefore, a high height of the satellite has a huge impact on the smoothness of the data in gravitational potential, while its impact is smaller for the gravitational tensor. Table 2.1 shows the final values for σ, λ and height for different gravity components. The weights are shown such that the order of magnitude is in the same range as the noise on the observations. λ is dependent on this using the relationships shown in Figure 2.4.

As can be seen in both Figure 2.3 and Figure 2.6, the root-mean-square (RMS) values for the error do not reach 0 kg/m^3 for any of the runs. This is because of the noise on the observations and the approximations made during the process, e.g. by the GSH tool. Even the results with the lowest RMS show a random pattern of density errors. These errors are deemed insignificant, as they do not correlate to any geological features or gravity signals.

This one-layer inversion was also used to study the effect of changing input parameters like the crust-mantle boundary, the elastic lithospheric thickness (Te) and the crustal density (D_c). Using synthetic planets, different crust-mantle boundaries were created using the topography and the Airy, infinite plate and thin shell isostatic adjustment theories. The input model used a different crust-mantle boundary than the observation ('true') model. Performing this with all combinations of the three crust-mantle boundaries, it was found that performing the inversion with a wrong crust-mantle boundary does not influence the stability of the inversion. The final results will be slightly less accurate than with the correct crust-mantle boundary, but it will still converge to the correct density pattern.

Then, a heat map as shown in Figure 2.7 was created using Te and D_c. The observation

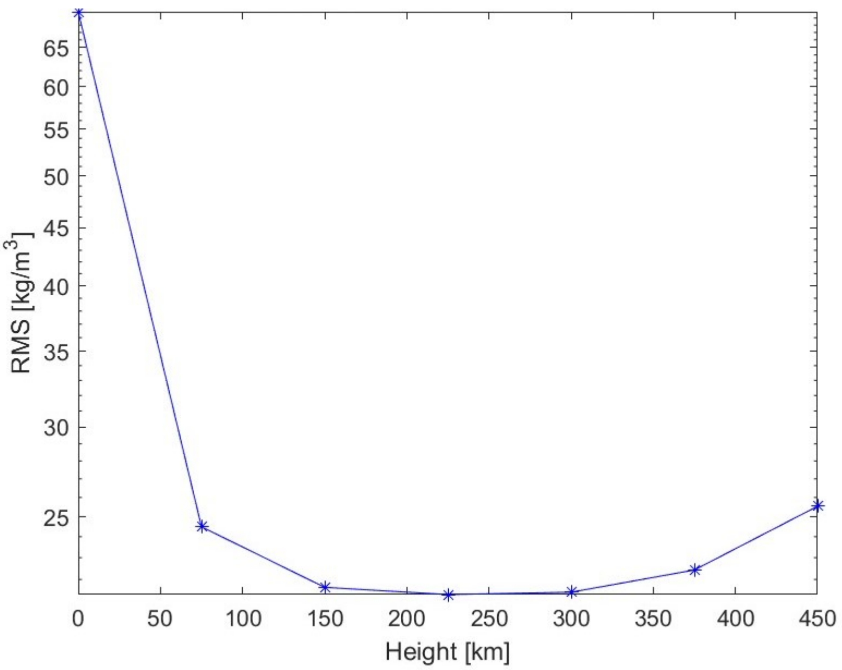

Figure 2.6: A height analysis for an inversion using the gravitational potential with $\sigma = 1e-1$, $\lambda = 1e-4$. On the y-axis the root-mean-square of the density error is depicted. Note that it is a logarithmic scale.

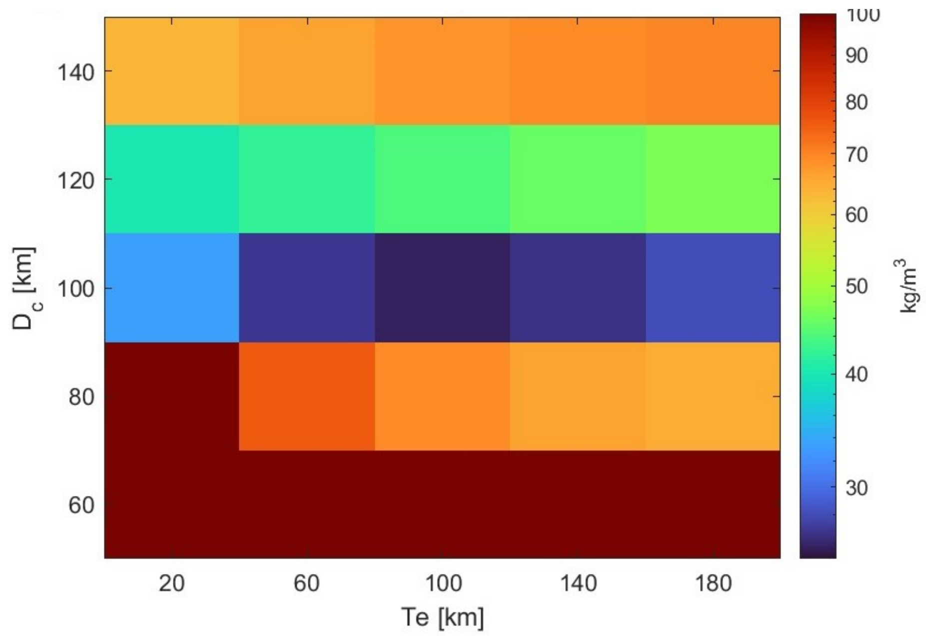

Figure 2.7: A heat map of a one-layer inversion using different values for Te and D_c. Note that the color bar is cut-off at 25 and 100 kg/m^3, and uses a logarithmic scale.

model is created with $Te = 100$ km and $D_c = 100$ km, while the model used for the inversion uses the values on the x- and y-axis. It can be seen that the result of the inversion is affected more by different values of D_c then Te. The best result is occurring for the values of D_c and Te that match the true values of the input model. From this plot, one can conclude that using the correct value for D_c is of greater importance than the correct value of Te.

All conclusions that are drawn within this chapter using the one-layer inversion, are applied to the two-layer inversion as described in chapter 3.

3
Journal article

On the next page, the journal article will start.

Astronomy & Astrophysics manuscript no. output
March 22, 2024

Two-layer gravity inversion on Mars

Three different inversion methods to obtain a global density model of the crust and upper mantle of Mars

F.M. van den Bogaard[1] and B.C. Root[1]

Aerospace Engineering, Delft University of Technology, Kluyverweg 1, 2629HS, Delft

Received 22 March 2024

ABSTRACT

The origin of the Martian dichotomy is subject to question and no substantial evidence exists. Some surface and interior features that are not visible in, e.g., topography data, can show up in gravity data. Therefore, this research inverts gravity data to find a crustal and mantle global density model. Previous research performed a one-layer inversion, assuming equal mass in all columns. Also, missions like InSight do not provide global interior information, but only at the landing site. The aim of this research is to provide a global density model of both the Martian crust and upper mantle. The inversion is performed using a weighted, regularized least-squares algorithm. The gravity input consists of the residual between the MRO120F data set and the state-of-the-art gravity field model of the TU Delft. The design matrix is built using Green's functions, which define the influence of a mass element in all different directions on a measurement point. Using this least-squares algorithm, three different methods for inversion are used. The separate two-layer inversion, the combined independent two-layer inversion and the combined dependent two-layer inversion. All three inversion methods are performed on synthetic planets as well, for verification purposes. By performing all inversions on the synthetic planets, it was found that the combined independent two-layer inversion results in a strong decoupling of short and long wavelength signals, but is not able to attribute gravity signals to different features in the crust and mantle. The combined dependent two-layer inversion does lead to a result that shows decoupling of crust and mantle features. The hypothesis is that adding different gravity components to the combined dependent two-layer inversion will further increase its accuracy. The results of the inversion methods applied to Mars are in agreement with existing research in terms of standard deviations of the crust and mantle density anomalies. The maps were also analysed geologically, where the most important conclusion is the evidence of potential impact basins in the north polar region. These can be evidence to accept the several impact theory for the origination of the Martian dichotomy. Increasing the resolution and refining the third inversion method with multiple gravity components will increase the potential of gravity inversion to define geological features of Mars.

Key words. Mars – Gravity field – Inversion – Two-layer interior model – Global crustal density – Global mantle density

1. Introduction

Exploring the Martian interior is paramount to unraveling the planet's geological history, its present conditions and the potential evidence of (ancient) water on Mars. In 1965, the first successful flyby of Mars was performed by Mariner 4, a spacecraft of NASA (Sloan 1968). Since this moment, enormous amounts of data have returned by multiple spacecraft and landers that are defining our understanding of Mars. However, still a lot is unknown.

Geologically, the Martian history can be divided into three main periods (Carr & Head 2010). The first of these periods, the Noachian epoch, started around 4.1 GYr ago and ended around 3.7 GYr ago. The Martian terrain that dates back to the Noachian epoch is characterized by the bombardment era. This results in heavily cratered surface features, covering about 40% of the surface of Mars. Before the Noachian period, already a big geological event happened: the global dichotomy. After the fairly quick accretion of Mars after the Solar System formation, Mars' northern and southern hemispheres started showing differences (Zuber et al. 2000) (Carr & Head 2010). This so-called dichotomy boundary does not exactly coincide with the northern and southern hemisphere, but does follow it approximately. The Martian topography, including the dichotomy and other important geological features, is shown in Figure 1.

The Martian dichotomy is visible in three characteristics. First, the dichotomy is present in the different elevations of the two hemispheres: the southern hemisphere is elevated around 5.5 km more than the northern hemisphere (Aharonson et al. 2001). The dichotomy is also present in the thickness of the crust: the northern hemisphere seems to have a thinner crust, being around 30 km, than the southern crust, being around 60 km thick (Neumann et al. 2004). Thirdly, the dichotomy is present in the crater count. The southern hemisphere is more heavily cratered than the north, however it could be the case that the surface north of the dichotomy boundary is covered by younger deposits and therefore showing less cratering. There is still a lot of uncertainty about the timescale and mode of formation of this dichotomy. Large impacts (McGill 1989), global mantle convection or tectonics (Sleep 1994) are all formation theories that are studied, but there is no definite conclusion (Carr & Head 2010) . Also, as Mars is a very active planet it is hard to study the surface conditions during the dichotomy period, as the geologic record has been almost completely erased.

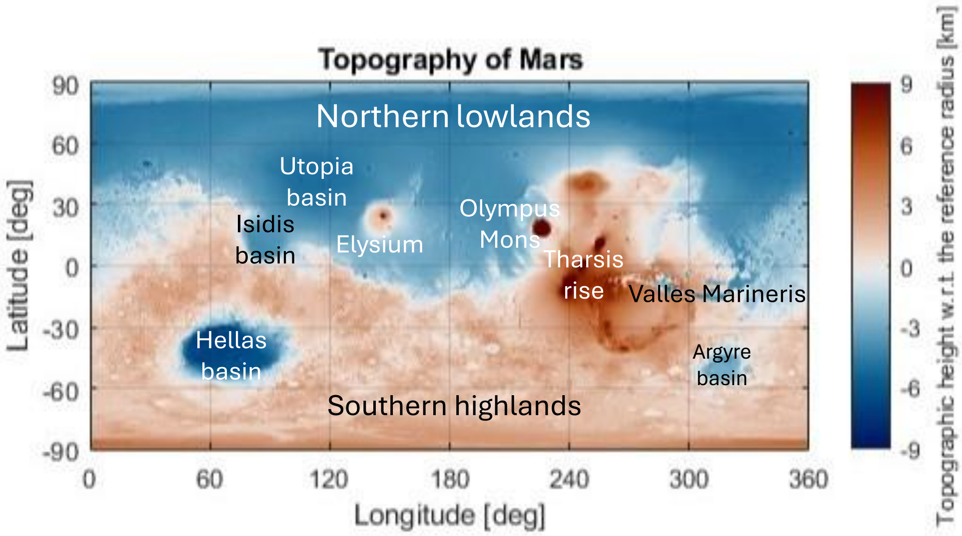

Fig. 1: The topographic map of Mars, retrieved from MOLA data `https://pds-geosciences.wustl.edu/missions/mgs/megdr.html`, last accessed on 29 August 2023. Important geological features are labelled.

After the first flyby of Mariner 4 in 1965, a multitude of other flyby's, orbiting satellites and landers have performed missions to Mars. Before the Mars Insight Lander (landed in November 2018), the Martian gravity field derived from all the different data was used to determine geological properties of Mars. Multiple studies show that the crustal thickness of Mars lies between 30 and 80 km, with an assumed density of around 3200 kg/m^3 (Wieczorek & Zuber 2004) (McGovern 2004) (Belleguic et al. 2005) (Neumann et al. 2004)). However, some studies also retrieve a crustal thickness of bigger than 100 km using the same crustal density assumptions (Baratoux et al. 2014) (Pauer & Breuer 2008). These density values are mean values, such that the variations might be in the range of +-300 kg/m^3. After the landing of InSight in Elysium Planitia in November 2018, researchers were able to better determine the internal structure at the landing site, but not necessarily on other locations on Mars. Multiple studies, like Knapmeyer-Endrun et al. (2021), Liang et al. (2022), Wieczorek et al. (2022), Durán et al. (2022) and Kim et al. (2023), used the seismometer on board of InSight to determine the crustal structure at Elysium. Generally, a crustal thickness ranging from 20 to 72 km was found, with a mean density of 2850-3100 kg/m^3. This agrees with the research pre-InSight. However, it disagrees with the possibility of a crust as thick as 110 km, or a mean crustal density as high as 3300 kg/m^3. The elastic thickness of the layer beneath the crust, the lithosphere, however, is less well constraint. Studies are performed using elastic lithosphere thicknesses ranging from 28 km (Zhong et al. 2022) to 210 km (Ding et al. 2019) and in between (e.g. McGovern (2004), (Comer et al. 1985) and (Ritzer & Hauck 2009)).

Previously, it was assumed that the northern hemisphere was a younger surface due to crater counting (Hartmann & Neukum 2001). However, with studying the gravity field of Mars, it might be possible to determine geological features like quasi-circular depressions. These quasi-circular depressions (QCD's) are thought to be old craters that have been buried with a layer of sediment. Therefore, they do not show up in topography data, but might show up in gravity data (Buczkowski et al. 2005). These QCD's are mostly occurring in the northern hemisphere. If these proposed QCD's indeed are buried craters, this changes the crater counting and could prove that the northern hemisphere is in fact older than the southern hemisphere. This shows that by analysis of gravity data, the geology of Mars can be better understood. The observed gravity field is the combination of surface relief, relief along the Moho (crust-mantle boundary) and relief within the mantle and the core. This allows for a geological interpretation of the gravity field. Thus, the gravity field can reveal geologic processes such as impact craters, volcanism and other subsurface structures (Wieczorek et al. 2022).

Two typical methods to use gravity data are forward modelling and inversion. They are opposite to each other. Forward modelling uses a known model and known input parameters to compute the gravity anomalies, such that these can be compared to the actual gravity observations. Gravity inversion uses a known model and the observed gravity anomalies, to compute the input parameters that best fit the inversion. In this case, the input parameters (e.g. crustal density) of the interior model are not yet known. Therefore, gravity inversion will be used.

This research is a follow-up on van Brummen (2022), presenting novel inversion methods using gravity data. In van Brummen (2022), a two-layer model of Mars is presented, however the inversion is only performed on one layer assuming an equal mass in all columns. In this research, we aim to provide the reader with a two-layer inversion, where the gravity data is used to decouple the crustal and upper mantle density variations. We are using three different methods for this, which are called a *separate two-layer inversion*, *combined independent two-layer inversion* and a *combined dependent two-layer inversion*. All use the same basic least-squared algorithm, being a weighted, regularized approach. This approach was in need of a thorough sensitivity analysis on the combination of several input parameters in the inversion. By performing this analysis, we defined a more reliable and stable inversion method. Also, this lowers the amount of assumptions needed to create a viable inversion method.

2. Methodology

As presented in the introduction, three different inversion methods will be used in this research. However, first the data sets used

Table 1: Martian interior parameters as used by the planetary exploration group of the TU Delft

Variable	Value
Elastic lithospheric thickness (Te)	104 km
Crustal density (ρ_c)	3050 kg/m^3
Mantle density (ρ_m)	3500 kg/m^3
Crustal depth (D_c)	60 km
Young's modulus (E)	100 GPa
Poisson ratio	0.30

in this research are presented, together with the Matlab tools. Then, the general least-squares approach is present. The three different inversion methods are presented last.

2.1. Data sets and processing tools

This research uses the MOLA topography dataset, revised by Wieczorek (2015) to create the commonly-used MARSTOPO2600. It can be retrieved from `https://pds-geosciences.wustl.edu/missions/mgs/megdr.html` (last accessed on 29 August 2023). As for gravity data, the MRO120F set will be used (`https://pds-geosciences.wustl.edu/mro/mro-m-rss-5-sdp-v1/mrors_1xxx/data/shadr/`, last accessed on June 13 2023) . This data set was developed by Konopliv et al. (2020) and uses data from several Mars missions, including MGS and MRO. This dataset goes up to spherical harmonic degree 120. However, the error of the measurements gets bigger than the signal of the measurements itself around degree 100. Therefore, we cut off the data at spherical harmonic degree 90, corresponding to surface features of hundreds of kilometers. This means that smaller-scale features, like small impact basins, might not be recognised using this approach.

The MRO120F data set is processed using the Global Spherical Harmonic (GSH) tool defined by Root et al. (2016), consisting of GSHA and GSHS. The Global Spherical Harmonic Analysis (GSHA) code analyses the planet layer by layer, converting each layer into a set of spherical harmonic coefficients to retrieve the spherical harmonic representation. This set of spherical harmonics can be translated by the Global Spherical Harmonic Synthesis (GSHS) to calculate the grids of the gravity vectors, gravitational potential and tensor fields. This toolbox is not only used to process the MRO120F data, but also to derive the gravity field of the obtained density variations after inversion.

Figure 2 visualises the MRO120F dataset, together with the Martian gravity model as it is modelled by the planetary exploration group of the TU Delft. This model includes flexural isostasy, as studied and modelled by Qin (2021) and the mantle plume underneath Tharsis as studied by van der Tang (2021). Table 1 shows the parameters that are used for this interior model. The bottom figure in Figure 2 shows the residual between the actual gravity field and the modelled gravity field. This is the residual that will be used in this study. Especially around Utopia, Hellas and Elysium clear differences with the gravity observations can be seen. It must be noted that the MRO120F gravity field and the modelled gravity field are corrected for spherical harmonic terms C_{00}, C_{10}, C_{11}, C_{20} and S_{11}.

The final Mars model used in this study is combining Table 1 with the MOLA topography. Figure 3 shows this interior model. It defines the bounds of the two layers, with the crust-mantle boundary being defined by the topography and the thin-shell flexure theory as studied by Qin (2021). The bottom of the second layer is constant, using a mantle thickness of 100 km.

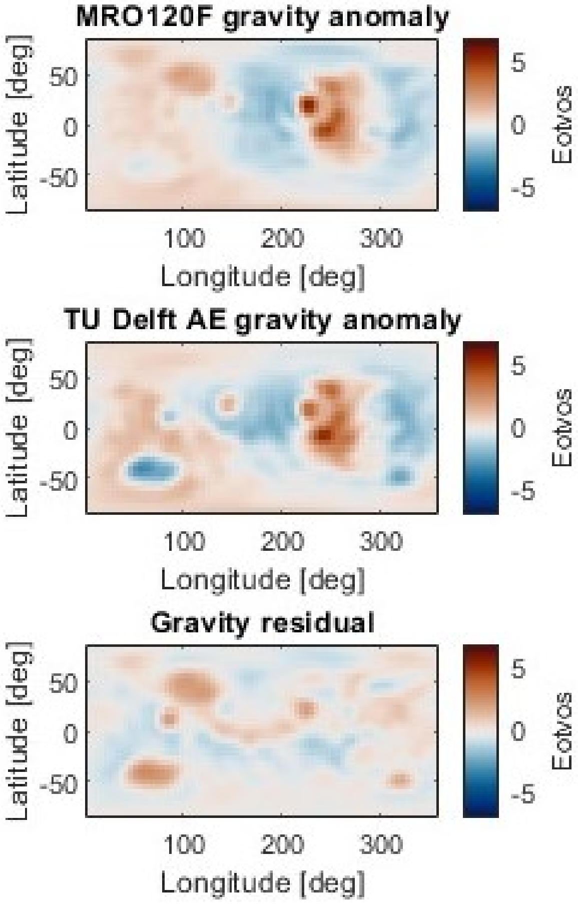

Fig. 2: The gravity anomaly as described by MRO120F (top figure), the TU Delft Aerospace Engineering planetary exploration group (middle figure) and the residual resulting from these two gravity models (bottom figure). The gravity models are corrected for C_{00}, C_{10}, C_{11}, C_{20} and S_{11}.

2.2. Least-squares approach

In this research we used a weighted, regularized least-squares approach, where the solution is of the form

$$\hat{x} = \left(A^t P_{yy}^{-1} A + \lambda I\right)^{-1} A^t P_{yy}^{-1} \bar{y}. \tag{1}$$

Here, $\hat{x}$ is the solution matrix, in this case containing the density values of the inverted layer. A is the design matrix, built using the Green's functions, which is further elaborated upon in subsection 2.3. Matrix P_{yy} is the covariance matrix, describing the correlation between the observations. In this case, it is defined as $P_{yy} = \frac{1}{\sigma^2}$, with σ being the weights of the observations. $\bar{y}$ is the observation matrix, containing the gravity field measurements. λ is the Tikhonov regularization parameter, adding a form of ridge regression. A regularization can be used to balance the norm of the residuals and the solution. The value of the Tikhonov parameter can differ greatly in different cases (i.e. 10^{-10} to 10^{10}).

Next to the big range of possible values for λ, its value is dependent on the weights (σ). Therefore, an analysis on the best fitting value for λ was performed. Using a synthetic planet (as

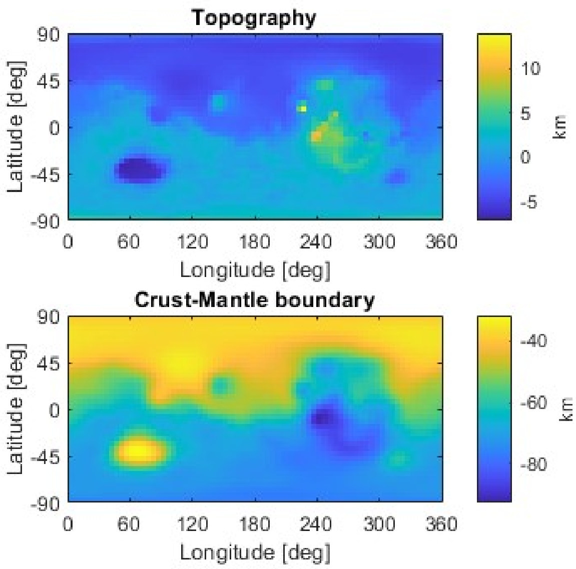

Fig. 3: Topography and crust-mantle boundary for the Mars interior model

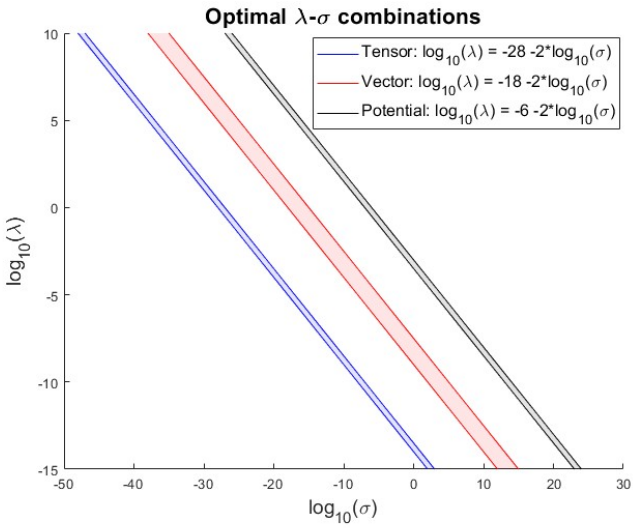

Fig. 4: The optimal combinations for λ and σ to be used in the weighted, regularized, least-squares problem. Described for all three gravity components.

Table 2: Final input values for σ, λ and height of satellite observations to be used in the least-squares algorithm

Gravity component	σ	λ	Height [km]
Tensor	10^{-10}	10^{-7}	100
Vector	10^{-5}	10^{-5}	100
Potential	10^{-3}	10^{5}	100

further explained in subsection 2.5), wide ranges of λ-σ combinations were tested for a one-layer inversion. We found that there exists a linear optimal combination between λ and σ. This relationship is shown in Figure 4. Here, the areas that are shown for the gravitational tensor, vector and potential are the most optimal combinations, however combinations shifting with an order of magnitude 2 (bigger and smaller) will yield to correct results as well. It can be seen that the optimal space for the gravitational vector is slightly wider. This implies that the vector is less prone to changes in σ and λ. For this research, we decided to choose values for σ that are in the order of magnitude of the noise of the data, which are shown in Table 2, together with its associating λ-values.

Next to this, during the sensitivity analysis it was found that the one-layer inversion is also very prone to changes in the height of the satellite observations in the GSH tool. This dependency also differed per gravity component. As the gravitational tensor is more prone to the distance of the measurement to the geological feature than the gravitational potential, its behaviour at different observation heights is also different. The optimal height for the one-layer inversion per gravity component is shown in Table 2.

Next to the quantitative analysis of λ, σ and height, a qualitative analysis of its behaviour outside of the optimal ranges is important in order to interpret the results when applying the method to Mars. For a λ-σ combination below the optimal linear combination, the noise on the observation data has too much influence and induces polar instabilities in the inversion. Above the optimal combinations, where the regularization parameter is bigger than the optimal combination with the weights, the inversion does not produce any output. This is because the inversion is then dominated by the regularization and that gravity observations are not sensed by the least-squares algorithm.

2.3. Green's function

Gravity can be represented in three components: the gravitational potential (V, existing in one direction with unit m^2/s^2), the gravity vector (g, commonly used description of gravity, existing in the three directions x, y and z, with unit m/s^2) and the gravitational tensor (Γ with unit $1/s^2$ and available in all combinations of the spherical coordinates (r, θ, ϕ)). This can also be described as

$$\Gamma = \text{gradgrad}V. \tag{2}$$

In order to define how a geological feature influences all the different components of the gravitational tensor, Martinec (2014) defined the so-called Green's functions $G(\bar{r}, \bar{r}') = \frac{1}{L(\bar{r}, \bar{r}')}$, with $\bar{r}$ and $\bar{r}'$ describing the distances to the geological feature and the measurement point respectively. Following the approach of Martinec (2014), the different tensors can be combined into three kernels, K_{rr}, $K_{r\Omega}$ and $K_{\Omega\Omega}$. These isotropic kernels are shown in Figure 5. It shows that the vertical-vertical kernel (K_{rr}) has the most impact when the topographic feature is right beneath the computation point, and the further away (with ψ) the mass occurs, the less influence it has on the vertical-vertical gradient. For the vertical-horizontal kernel ($K_{r\Omega}$) this is not the case. Here, the features with a small non-zero angular degree have a greater impact than for $\psi = 0$ or larger values of ψ. This is also the case for the horizontal-horizontal kernel ($K_{\Omega\Omega}$), for which the peak is smoothed out (w.r.t. the curve of $K_{r\Omega}$). One can expect that the closer the measurement point is to the observed mass, the more impact all kernels will have. Especially, the K_{rr} kernels become relatively strong (Martinec 2014) compared to the other kernels. The behaviour and impact of the different kernels also changes with the height of the computation point.

If one determines the mass element of interest, and assumes a constant density within the mass element i, the gravitational gradient tensor in the vertical-vertical direction can be expressed

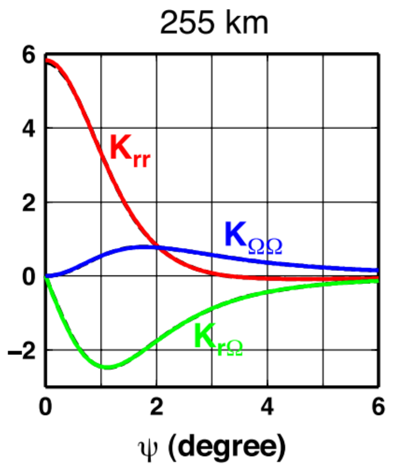

Fig. 5: This figure, obtained from Martinec (2014), shows the isotropic kernels K_{rr}, $K_{r\Omega}$ and $K_{\Omega\Omega}$ as a function of the angular distance ψ and at a height of the computation point of 255 km. For this figure the radius of the Earth is used.

as

$$\mathbf{\Gamma}_{rr} = \frac{G}{r^3}\rho_i K_{rr,i} V_i, \tag{3}$$

with ρ_i and V_i being the density and volume of the mass element of interest, respectively. Now, this needs to be related back to the linear least-squares problem $\hat{x} = \left(A^t P_{yy}^{-1} A + \lambda I\right)^{-1} A^t P_{yy}^{-1} \bar{y}$. As the volume of the mass element considered is known, ρ is the unknown parameter that needs to be solved for, giving $\bar{x}_{rr} = \rho$. Then, the design matrix can be defined as $A_{rr} = \frac{G}{r^3} K_{rr} V$, with r being the distance between the mass and the computation point. Now, A and $\bar{x}$ also need to be determined for the isotropic kernels in other directions. This can be done in the same way as for Γ_{rr}, giving the following design matrices:

$$A_{rr} = \frac{G}{r^3} K_{rr} V, \tag{4}$$

$$A_{r\theta} = 2\frac{G}{r^3} K_{r\Omega} \cos(\alpha) V, \tag{5}$$

$$A_{r\phi} = -2\frac{G}{r^3} K_{r\Omega} \sin(\alpha) V, \tag{6}$$

$$A_{\theta\theta} = \frac{G}{r^3} K_{\Omega\Omega} \cos(2\alpha) V, \tag{7}$$

$$A_{\phi\phi} = \frac{G}{r^3} K_{\Omega\Omega} \cos(2\alpha) V, \tag{8}$$

$$A_{\theta\phi} = -2\frac{G}{r^3} K_{\Omega\Omega} \sin(2\alpha) V. \tag{9}$$

α denotes the azimuth angle. The different factors that appear in these design matrices are based on Figure 5 and described by Martinec (2014). Constructing a full design matrix A is not as simple as adding up all these partial design matrices. The full gravitational tensor is defined as

$$\Gamma = \Gamma_{rr} + \Gamma_{r\Omega} + \Gamma_{\Omega\Omega} = D_{rr}\left(\mathbf{e}_{rr} - \frac{1}{2}(\mathbf{e}_{\theta\theta} + \mathbf{e}_{\phi\phi})\right) + \left(2D_{r\theta}\mathbf{e}_{r\theta} - 2D_{r\phi}\mathbf{e}_{r\phi}\right) + \left(D_{\theta\theta\phi\phi}(\mathbf{e}_{\theta\theta} - \mathbf{e}_{\phi\phi}) - 2D_{\theta\phi}\mathbf{e}_{\theta\phi}\right). \tag{10}$$

Now that the different components of the design matrix A are determined, the observation matrix y can be defined, using the subscript i, where 1 is the first observation point and I the last. Using the gravitational tensor, this gives:

$$\bar{y} = \begin{bmatrix} \Gamma rr,1 \\ \vdots \\ \Gamma_{rr,I} \\ \Gamma_{r\theta,1} \\ \vdots \\ \Gamma_{r\theta,I} \\ \Gamma_{r\phi,1} \\ \vdots \\ \Gamma_{r\phi,I} \\ \Gamma_{\theta\theta,1} \\ \vdots \\ \Gamma_{\theta\theta,I} \\ \Gamma_{\phi\theta,1} \\ \vdots \\ \Gamma_{\phi\theta,I} \\ \Gamma_{\theta\theta,1} \\ \vdots \\ \Gamma_{\theta\theta,I} \end{bmatrix}, \tag{11}$$

such that it has the shape $(6i, 1)$. Now, output matrix $\bar{x}$ is defined as

$$\bar{x} = \begin{bmatrix} \rho_1 \\ \vdots \\ \rho_i \end{bmatrix}, \tag{12}$$

thus having a shape of $(i, 1)$. Finally, the design matrix A_Γ is constructed using Equation 4 through Equation 9 and Equation 10 as follows:

$$A_\Gamma = \frac{G}{r^3}\begin{bmatrix} K_{rr,1}V_1 & \dots & K_{rr,1}V_I \\ \vdots & & \vdots \\ K_{rr,I}V_1 & \dots & K_{rr,I}V_I \\ -\frac{1}{2}K_{rr,1}V_1 & \dots & -\frac{1}{2}K_{rr,1}V_I \\ \vdots & & \vdots \\ -\frac{1}{2}K_{rr,I}V_1 & \dots & -\frac{1}{2}K_{rr,I}V_I \\ 2\cos\alpha K_{r\Omega,1}V_1 & \dots & 2\cos\alpha K_{r\Omega,1}V_I \\ \vdots & & \vdots \\ 2\cos\alpha K_{r\Omega,I}V_1 & \dots & 2\cos\alpha K_{r\Omega,I}V_I \\ -2\sin\alpha K_{r\Omega,1}V_1 & \dots & -2\sin\alpha K_{r\Omega,1}V_I \\ \vdots & & \vdots \\ -2\sin\alpha K_{r\Omega,I}V_1 & \dots & -2\sin\alpha K_{r\Omega,I}V_I \\ -2\sin 2\alpha K_{\Omega\Omega,1}V_1 & \dots & -2\sin 2\alpha K_{\Omega\Omega,1}V_I \\ \vdots & & \vdots \\ -2\sin 2\alpha K_{\Omega\Omega,I}V_1 & \dots & -2\sin 2\alpha K_{\Omega\Omega,I}V_I \\ 2\cos 2\alpha K_{\Omega\Omega,1}V_1 & \dots & 2\cos 2\alpha K_{\Omega\Omega,1}V_I \\ \vdots & & \vdots \\ 2\cos 2\alpha K_{\Omega\Omega,I}V_1 & \dots & 2\cos 2\alpha K_{\Omega\Omega,I}V_I \end{bmatrix}, \tag{13}$$

resulting with a shape of $(6i, i)$.

The same procedure can also be followed when constructing the design matrices for the gravitational vector and the gravitational potential. For these gravity components, the design matrix will result in a shape of $(3i, i)$ and (i, i), respectively. Thus, if one would incorporate all gravity components in the least-squares algorithm, the final design matrix has the shape $(10i, i)$

2.4. Three inversion methods

Using the linear, weighted, regularized least squares approach and the definition of the design matrix as described previously, several inversion methods can be built. In this research, three methods are tested. All of them use the same baseline, which is shown in Figure 6. In this flowchart, it can be seen that before the actual inversion happens, all the data en settings need to be prepared. The gravity residual should be calculated (as also shown and explained by Figure 2), the interior model should be defined (see Table 1) and the inversion settings should be chosen (Table 2). Thereafter, the inversion itself can be performed. In the next sections, we will elaborate on the three inversion methods that are used in this research.

2.4.1. Separate two-layer inversion

This inversion method uses the initial gravity residual as input for the crustal density. Using the new crustal density variations, the updated gravity field is calculated. Then the new gravity residual can be computed, which is used as the input for a mantle inversion. Now, the updated interior model has density variations in both the crust and the mantle. Again, using the GSH tool the gravity field of this interior model is calculated, leading to a new gravity residual. This gravity residual is used as input for the crust. The next iteration, the new gravity residual is used as input for the mantle, etc. The name of this inversion arises from the fact that this method does not invert the two layers together, but separate from each other. Per iteration, the input parameters of the inversion can be chosen. For example, one can invert the crustal layer using the gravitational potential, while the mantle

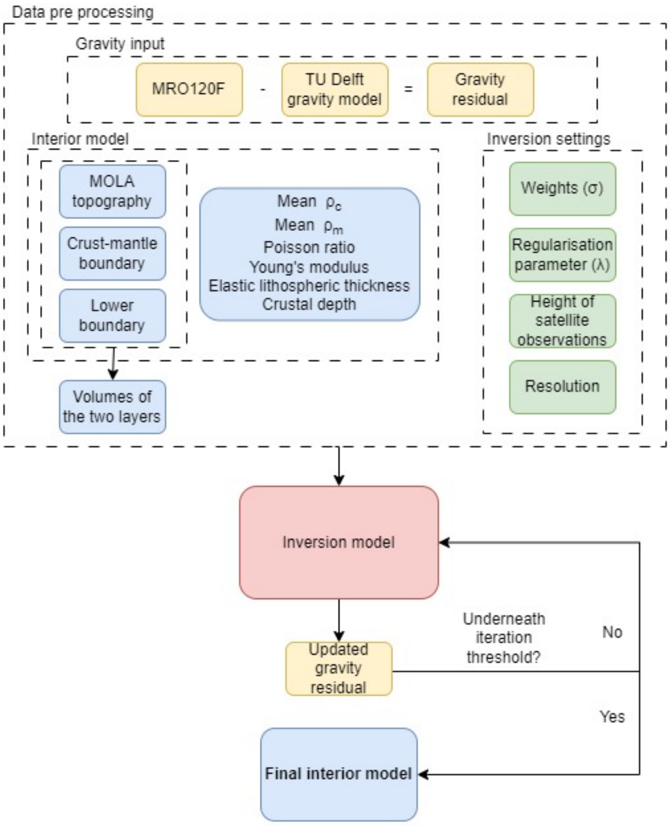

Fig. 6: A schematic overview of the baseline of all three inversion methods

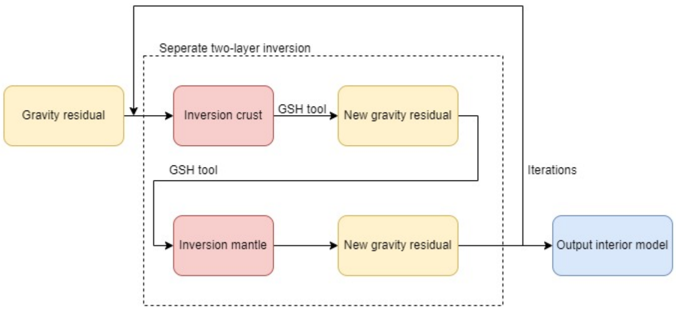

Fig. 7: Flowchart of the separate two-layer inversion scheme

layer can be inverted with the gravitational tensor. The gravitational potential (m^2/s^2) is more prone to the height of the observations. This allows for a decoupling between long wavelength signals and short wavelength signals. However, the downfall of this method might be that gravity signals that are originally arising from mantle density variation are attributed to the crust in the first iteration. One could also choose to start the inversion with the mantle, and then use the remaining gravity residual for the crustal inversion. Figure 7 shows a flowchart of this inversion scheme.

2.4.2. Combined independent two-layer inversion

This inversion methods inverts the crust and mantle layer at the same time, leading to the name *combined*. Figure 8 shows a flowchart of this inversion scheme. The initial gravity residual

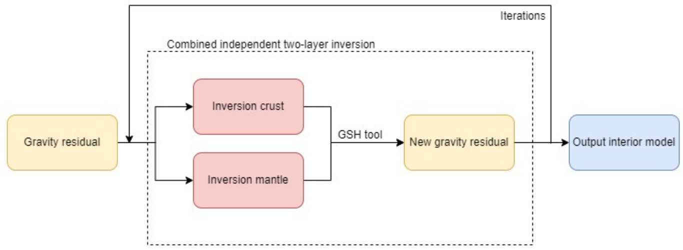

Fig. 8: Flowchart of the combined independent two-layer inversion scheme

is calculated as shown in Figure 6. This residual is then used to simultaneously invert the crust and mantle layer, by performing two parallel inversions. Both of these inversions can be tweaked independently, hence the name. Again, one might choose to invert the crust with the gravitational tensor while the mantle is inverted using the gravitational potential. For both inversions, the same gravity residual is used. Then, the new interior model with crustal and mantle density variations is used to compute the new gravity field. This will overshoot the initial gravity residual. Therefore, multiple iterations must be performed. The second iteration will use the new gravity residual to again simultaneously invert the crust and mantle. The next iteration will use the new gravity residual.

2.4.3. Combined dependent two-layer inversion

The third inversion method uses a somewhat different structure. For this inversion, both the crust and mantle are inverted simultaneously, but this time using a full design matrix, such that the inversion is performed only once, but is including both layers. The design matrix as presented in subsection 2.3 must therefore be altered slightly. For this inversion, the design matrix looks like $A_{tot} = [A_c\ A_m]$, where A_c and A_m are the design matrices as derived in subsection 2.3 using the kernels and volumes for each layer respectively. The subscripts c and m denote the crustal and mantle layer, respectively. This matrix is of the shape $(6i, 2i)$, thus the observation matrix also needs to be doubled such that it gets shape $(2i,1)$ instead of $(i,1)$. The observation matrix therefore has the shape

$$\bar{y} = \begin{bmatrix} y_{obs,1} & \dots & y_{obs,I} & y_{obs,1} & \dots & y_{obs,I} \end{bmatrix}^T. \quad (14)$$

This means that the same observations are used for both the mantle and crust inversion, but the design matrix is tailored to the respective layers. The output matrix $\hat{x}$ will be of the shape (2i,1), giving the crustal densities at all points i and mantle densities at all locations i. As this method simultaneously inverts both layers, but uses only one inversion matrix, the name *combined dependent two-layer inversion* arises. In this inversion, the weights (σ) used should be carefully considered. As all different gravity components are used, the weights should also be adaptable. Therefore, a weight matrix of the shape $[\sigma_\Gamma, \sigma_\Gamma, \sigma_\Gamma, \sigma_\Gamma, \sigma_\Gamma, \sigma_\Gamma, \sigma_g, \sigma_g, \sigma_g, \sigma_V]$ is defined, with $P_{yy} = \frac{1}{\sigma^2}$. For the value of λ, a general value corresponding to all different values of σ should be chosen. This can be done using the linear relationship between λ and σ as defined in subsection 2.2. Figure 9 shows a flowchart of this inversion scheme.

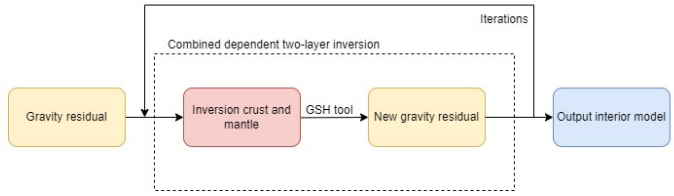

Fig. 9: Flowchart of the combined dependent two-layer inversion scheme

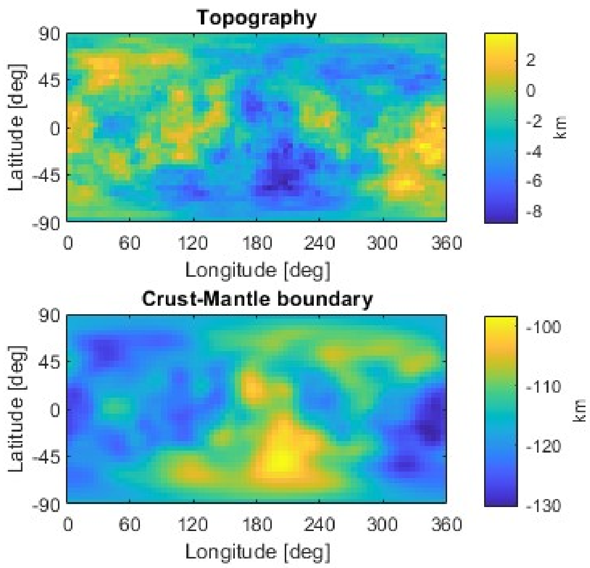

Fig. 10: Bounds as used for both of the synthetic planets

2.5. Synthetic planets

If you directly apply these three inversion methods to the Martian gravity field, it is not possible to verify the results of the crustal and mantle density variations. In order to test and verify the three different inversion methods, use can be made of synthetic planets. A synthetic planet is a planet of which all input parameters are known and resembles Mars in terms of topography and geological features. Using a synthetic planet creates an artificial set of gravity observations, of which the whole interior model is known. The settings of the inversion (e.g. crust-mantle boundary) can be chosen such that it perfectly resembles the synthetic planet, meaning that after inversion, the resulting gravity anomaly residual will exclusively represent errors arising due to the inversion method.

All three inversion methods are tested using two synthetic planets, using the Matèrn covariance function as explained in van Brummen (2022). Two versions of the synthetic planet are created: one for which the crust and mantle have similar features and one where the crust has predominantly short wavelength features and the mantle long wavelength feature. From previous research, it is expected that the upper mantle of Mars presents a smoother density variation pattern, while the crust can show fairly big and sudden variations. It is therefore expected that the second synthetic planet better resembles Mars. However, for verification purposes both synthetic planets are used. Also, an understanding of how these two different planets react to all three inversion methods will allow for a better understanding of the results that arise from using the Martian gravity field.

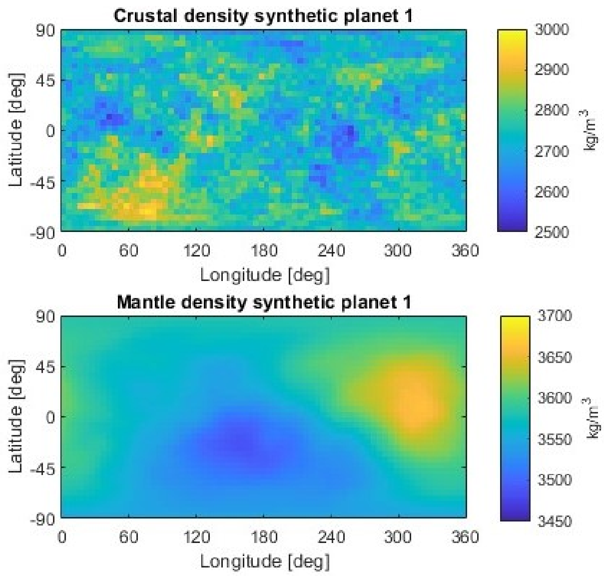

(a) Synthetic planet 1

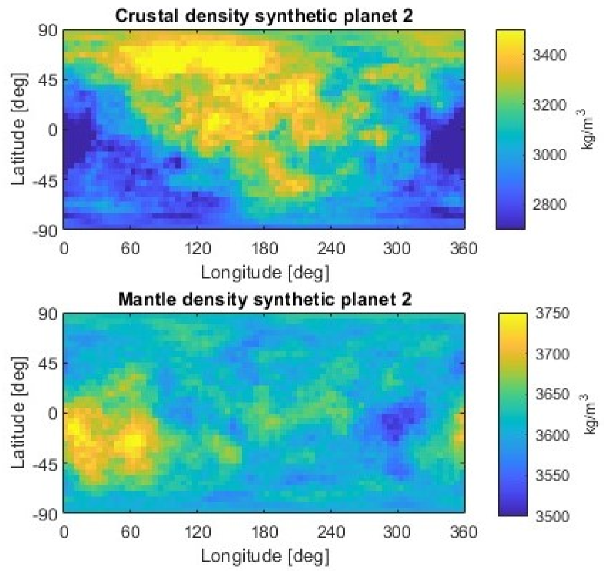

(b) Synthetic planet 2

Fig. 11: Crustal and mantle densities of both synthetic planets.

Both synthetic planets use the same topography, crust-mantle boundary and bottom bound (bottom of the mantle layer). Figure 10 shows the topography that was randomly created, together with a crust-mantle boundary that is based on the thin-shell flexure model from Qin (2021). The bottom bound of the second layer is taken as a constant value, with a mantle thickness of 100 km.

The two synthetic planets differ in their crustal and mantle densities, as explained before. Figure 11 shows the densities of the two layers. In both cases, the crustal density is much lower than the mantle density. Next to this, the standard deviation of the crustal densities are higher than the standard deviation of the mantle densities.

3. Results

All three inversions are performed for the synthetic planets and on Mars. In this section, all of these results will be presented. During this research, we found that the results for both synthetic planets were similar to each other. Therefore, only the results of synthetic planet 1 are presented in the main body of this paper. Appendix A elaborates on the second synthetic planet. For all inversions, both on the synthetic planets and on Mars, the final gravity residual is smaller than the iteration threshold. Therefore, these graphs are not included. The results of the crustal and mantle density anomalies of synthetic planet 1 are presented in Figure 12 and Figure 13. These figures also show the true density pattern of the synthetic planet again, allowing an easy comparison. In the next paragraphs, all of these results will be elaborated upon. After the results of the synthetic planets are presented, the results of performing the inversions on Mars are presented.

3.1. Separate two-layer inversion: Synthetic planets

In Figure 12b and Figure 13b the outputs of the separate two-layer inversion, performed on the synthetic planet, can be found. In this case, the crust is inverted using the gravitational tensor and the mantle is inverted using the potential. This is the combination that is best able to decouple gravity signals into two layers, as the tensor is less prone to height and distance than the potential. All other combinations of gravity components were also tested, but we concluded that this is the best combination. However, the difference between all of them is fairly small. Supplementing information on this can be found in Appendix B.

An important thing to notice is that there indeed seems to be some decoupling between the crust and the mantle: the output patterns are not the same. This means that different signals are going in the crust and the mantle, respectively. However, it is also clear that the output patterns are not resembling the true density patterns. As the crust is inverted first, most of this gravity signal is constrained to the crust. This is both the gravity signal due to the crust and mantle. The error that is left, is placed fully in the mantle.

As the crust is inverted using the gravitational tensor, its output consists of shorter wavelengths than the mantle, which was inverted using the potential. This is also what we see in the true density patterns. However, the long wavelengths in the mantle are not at all corresponding to the long wavelength patterns in the true mantle density map.

3.2. Combined independent two-layer inversion: Synthetic planets

This inversion results in an output crustal density map as presented in Figure 12c and an output mantle density map as presented in Figure 13c. It is clear that these present little to no decoupling of features. Both the crustal and mantle density maps show the same geological features as each other. As both layers are inverted at the same time, using the same information, it makes sense that both have the same output.

However, there is a distinct difference between the long and short wavelength features. In this inversion, the difference is so apparent that certain short wavelength features are only present in the crustal density anomalies and not in the mantle anomalies. For example, between longitudes 180° and 240° and latitudes -45 ° and -90° the true crustal density map shows positive anomalies that do not appear in the mantle density anomalies. These positive anomalies are only captured in the output of the crustal inversion, and not in the mantle inversion. This is due to the difference in inversion settings, where the crust uses the gravitational tensor and the mantle the gravitational potential.

In this inversion it becomes clear that as both the layers use the same gravity residual as input, the layers cannot behave dependent on each other. The inversion does not know which features to place in the crust and which features are coming from the mantle. It is solely able to constrain very short wavelength features to the crust.

3.3. Combined dependent two-layer inversion: Synthetic planets

In order to keep the runtime low, for this method a synthetic planet with a resolution 10° is used, instead of a 5° resolution as is used for the first two inversion methods. The same crustal density pattern as presented in Figure 10 is used, but the resolution has been scaled down to 10°. Also, the same topography, crust-mantle boundary and lower boundaries are used, but scaled down to a 10° resolution. Figure 12d and Figure 13d show the plots with the outputs of this inversion.

From first glance, no clear differences between the crustal and mantle results can be found. However, if one looks closer, decoupling can be distinguished. First, around the 0° - 10° longitude in the southern hemisphere the mantle shows a negative density anomaly, with the crust having positive anomalies up until latitude -70°. Next to this around 300° longitude and -45° latitude, the positive anomalies in the mantle continue to around 260° longitude, while this is not happening in the crust. In the north-western corner there is also a larger negative anomaly present in the mantle. This negative anomaly is also visible in the crustal density anomalies, however it is shaped more like a horizontal line and does not have a high contrast with respect to the positive anomalies surrounding this patch. In the north-east corner in the crustal density map, there is a clear positive density anomaly, presenting as a horizontal (lateral) line, extending from 240 ° to 250° longitude. This positive anomaly is also present in the mantle, but is not depicted as a lateral line with roughly the same values. Rather, it is visible at different positive values.

This inversion does not capture the difference between the long and short wavelength features. This is due to the fact that both layers are inverted with the same gravity component (namely the tensor). It is expected that when the potential is also incorporated in the inversion, the larger wavelengths can be captured using this component.

3.4. Intermediate conclusions on the inversion methods performed on a synthetic planet

From Figure 12 and Figure 13 and the observations as described in the previous sections, it can be concluded that none of the three inversion methods result in the true density patterns. However, especially with the combined independent and dependent methods, there are some things happening that can lead to interesting results when applying the methods to Mars. These include the decoupling of short and large wavelength features in the combined independent two-layer inversion and the small differences in crust and mantle patterns in the combined dependent two-layer inversion.

Another important thing that can be concluded from these results, is that all three methods are sensitive to the absolute range of density values . As seen in Figure 12a and Figure 13a, the crustal anomalies range between ± 400 kg/m^3, while the mantle anomalies range between ± 100 kg/m^3. The ranges of density anomalies in the crust and mantle for the three inversion methods correspond to these values.

3.5. Separate two-layer inversion: Mars

Figure 14 shows the outcome of the separate two-layer inversion on Mars, in terms of crustal and mantle densities. Of course, there is no true density map that it can be compared to. However, in Figure 14 it does seem like some decoupling is taking place, where the crust takes up all the shorter wavelength features while the mantle is more smoothed out and showing the larger wavelength features. Compared to the synthetic planet result, this shows more difference between short and large wavelengths. For example, some short wavelength features are not visible in the mantle densities. This can be seen in the negative rim around Utopia and Hellas basin that is present in the crustal density anomaly map and not in the mantle density map. Also, around Tharsis rise and Olympus Mons the mantle density map shows purely negative values, with the crustal density map showing small scale features with both positive and negative values. A final difference between the crust and mantle layer, is at the Argyre basin. There, the crust shows very high anomalies, while the mantle is smooth and does not show any higher anomalies at Argyre basin.

3.6. Combined independent two-layer inversion: Mars

In Figure 15 the results of the combined independent two-layer inversion applied to Mars is seen and it looks very similar to Figure 14. However, with this inversion method some severe edge effects are taking place in the south polar region. These edge effects can be due to a computational instability, or an instability due to the high amount of data points present in the poles. It was tested if different combinations of λ and σ help to get rid of these edge effects. This is not the case, so it is an instability of combining this gravity residual with this inversion method and the settings of the interior model. For the analysis of this result, the edge effects are further neglected and not analysed.

In contrary to the result of the synthetic planet, it is less clear that decoupling is taking place. Still, the crust shows small scale features, while the mantle shows larger scale features. However, there are no locations where the crust exhibits a significant difference compared to the mantle.

3.7. Combined dependent two-layer inversion: Mars

Finally, the third inversion was applied to Mars. The residual as presented in the previous two methods is used. After 15 iterations, the gravity residual is below the threshold. In Figure 16, the crustal and mantle densities are shown. The first noticeable thing, is that the resolution of 10° clearly leaves out the smaller scale features, thus those can not be analysed. Just like the synthetic planet analysis, no separation of large and small scale features are present as both layers use the tensor. However, especially around the Tharsis rise the crust and mantle maps show differences. The Tharsis rise itself shows a large negative anomaly in the crust, with the mantle showing a very mild negative anomaly in the southern part of Tharsis and a positive anomaly in the northern part of Tharsis. Next to this, Hellas, Utopia and Argyre basin show negative anomalies in both the crust and mantle.

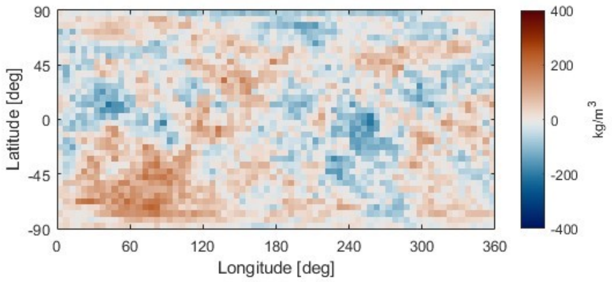

(a) Crustal density model of the synthetic planet

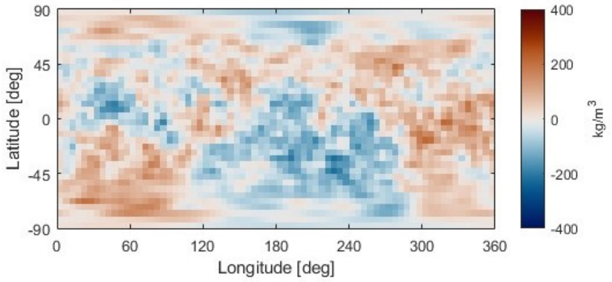

(b) Output of the crustal layer using the separate two-layer inversion

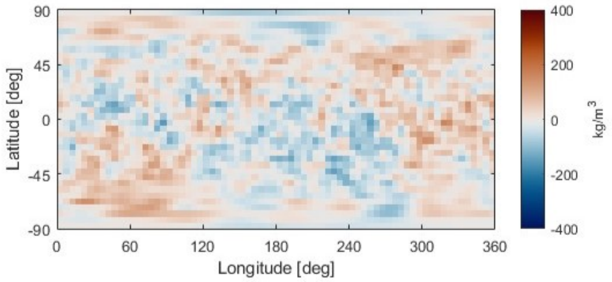

(c) Output of the crustal layer using the combined independent two-layer inversion

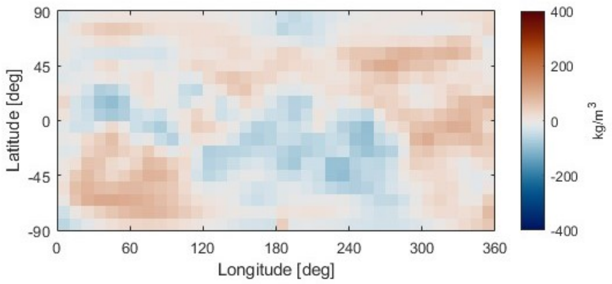

(d) Output of the crustal layer using the combined dependent two-layer inversion

Fig. 12: The true crustal density model and the outputs of all three inversion methods. All colorbars have the same limits (± 400 kg/m^3). The synthetic planet model and the first two inversion methods have a resolution of 5°, while the third inversion method uses a 10° resolution.

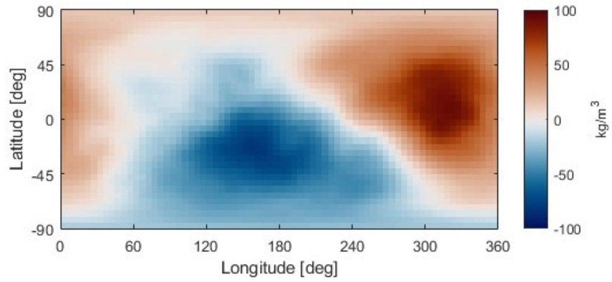

(a) Mantle density model of the synthetic planet

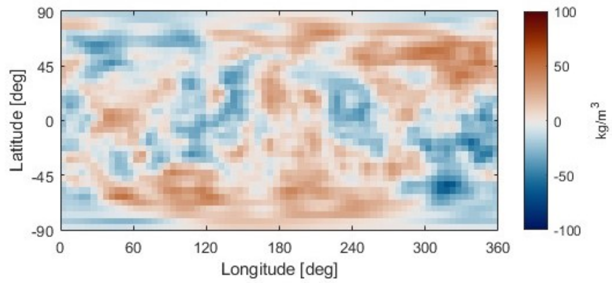

(b) Output of the mantle layer using the separate two-layer inversion

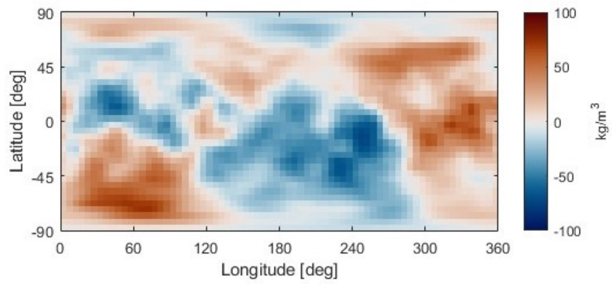

(c) Output of the mantle layer using the combined independent two-layer inversion

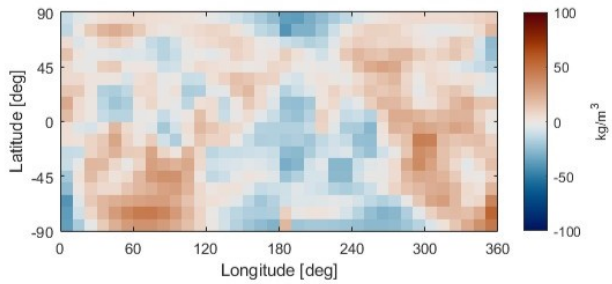

(d) Output of the mantle layer using the combined dependent two-layer inversion

Fig. 13: The true mantle density model and the outputs of all three inversion methods. All colorbars have the same limits (± 100 kg/m^3). The synthetic planet model and the first two inversion methods have a resolution of 5°, while the third inversion method uses a 10° resolution.

4. Conclusions

In this section, first the three inversion methods will be discussed. Conclusions are drawn on its stability and reliability. Also, concluding remarks on the Martian crust and mantle density profiles will be made.

It is fairly clear that neither of the first two inversion method yield a solution that agrees to the true interior model. The combined independent two-layer model does decouple long- and short wavelengths and puts the shorter wavelengths in the crust and longer wavelengths in the mantle, however this method does not allow for different features to be attributed to the crust or mantle. The separate two-layer inversion is, at first glance, able to do this, however, in the first iteration all features are constrained to the first layer that is inverted (in our case the crust). Per iteration, the method is not able to distinguish between crust and mantle features and puts all gravity signals in the layer that is inverted during that iteration.

Keeping this conclusion in mind, the results of the first two inversion methods performed on Mars can be concluded. The results for Mars show a stronger decoupling between short and long wavelength signals than the synthetic planets. This might be due to the gravity anomaly of Mars that is dominated with larger wavelength signals, but with very steep changes between each grid cell. Therefore, the extreme values go into the crust, with the remaining smoother, softer long-wavelength signals going in the mantle. Both the inversion methods show a relatively similar outcome. Based solely on the results of the first two inversion methods performed on Mars, it can be concluded that the crustal density of Mars is 3050±400 kg/m^3 with the main outliers being Hellas basin, Argyre basin, Olympus Mons and Isidis basin. The density of the upper mantle layer is 3500±200 kg/m^3, with the extreme values at Tharsis rise and Hellas basin.

The third inversion method, the combined dependent two-layer inversion, shows no clear differences in short and long wavelength features in the crust and mantle, but does show little differences in density patterns. This means that some signals from the gravity residual are placed in the crust and others in the mantle. This is a promising result, as it implies that more separation of gravity signals is possible when alterations to the inversion model are made.

Then, looking at the final inversion method performed on Mars, the density results do not show a clear decoupling between long and short wavelength features. This third result of Mars generally agrees to the results of Mars using the first two inversion methods: a stronger crustal density signal, compared to the mantle density map. From this inversion, the crustal density is slightly less extreme, resulting in 3050±350 kg/m^3 and a mantle density of 3500±150 kg/m^3.

In conclusion, the first two inversion methods show that a decoupling of short and long wavelength features is possible when using the gravitational tensor for the crust and the potential for the mantle. The third method shows that it is possible to attribute some gravity signals to the crust and others to the mantle. Combining these conclusions can lead to the possibility of using the third inversion method and including other gravity components to get the separation of short and long wavelength features.

5. Discussion and geological interpretation

From the last conclusion, the third inversion method can be discussed further. This inversion method only uses the gravitational tensor. However, in theory it is possible to include all three gravity components in the inversion. The limitation in this research

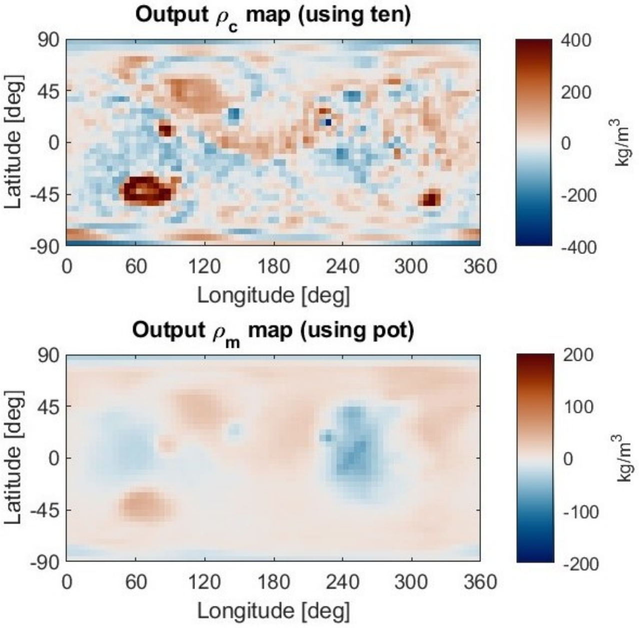

Fig. 14: Output density anomaly maps of the separate two-layer inversion performed on Mars

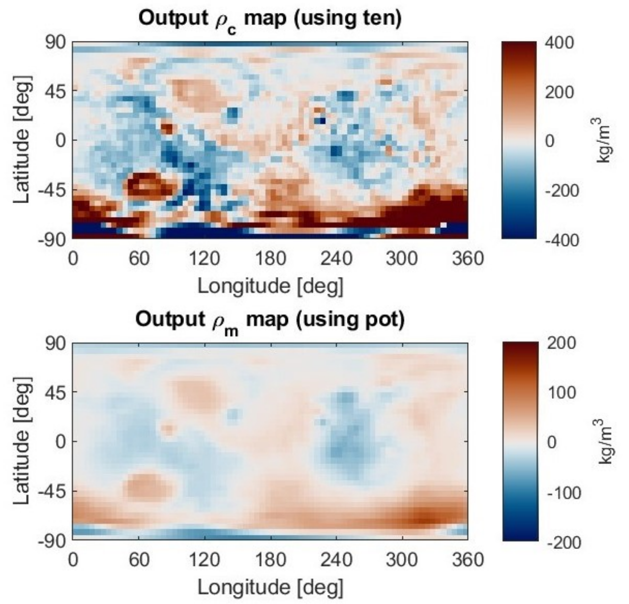

Fig. 15: Output density anomaly maps of the combined independent two-layer inversion performed on Mars

lies within the regularization parameter that could be assigned only one value. Therefore, performing the method with all gravity components would lead to an unstable combination of the weights and regularization parameter. Including a full matrix for the regularization matrix can lead to a stable conversion for all gravity components. Then, the results of the decoupling of short and long wavelengths of the first second inversion methods can be added to the third inversion, possibly leading to a more reliable global density model of Mars.

Although this research cannot conclusively determine the reliability of the Martian crustal and mantle density maps, the over-

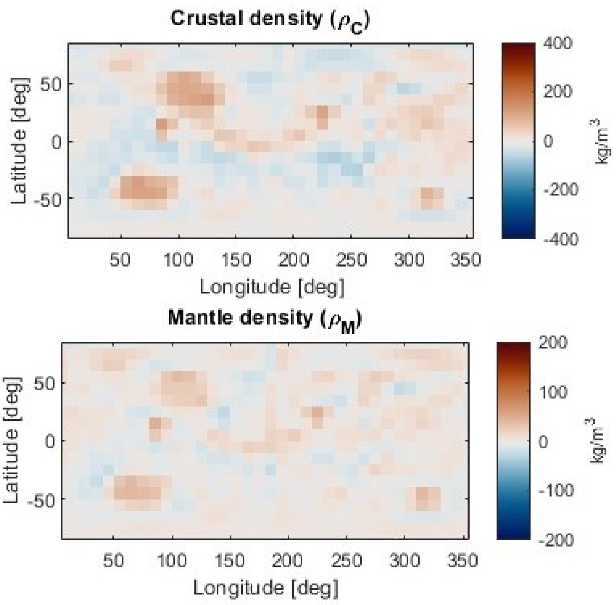

Fig. 16: Output density anomaly maps of the combined dependent two-layer inversion performed on Mars

all results of all three methods are so similar that a geological interpretation of these maps can be provided.

The global range of densities in both the crust and mantle does not contradict previous research, however no previous research has mentioned a potential crustal thickness at certain locations of 3450 kg/m^3 yet. However, as mentioned in the introduction multiple studies use mean crustal densities of around 3200 kg/m^3 (e.g. Wieczorek & Zuber (2004), (McGovern 2004)), with other studies showing that variations around this mean can be in the range of ± 300 kg/m^3 (Baratoux et al. 2014). Combining this, a maximum crustal density of 3450 kg/m^3 is acceptable.

An other global result is that the dichotomy is not visible in the crustal composition of Mars. This is consistent with findings from Pan et al. (2017), who shows that the crustal composition of the northern lowlands and the southern highlands are quite similar.

At the landing site of InSight, measurements on the density of the surface exist. These densities are around 1300 kg/m^3 (Drilleau et al. 2022), however this measurement only goes a few meters deep. Therefore, this value only shows that the top layer of the surface is covered by very light sediment. This value can not be compared to the density value found at this location in this study.

An interesting specific geological feature is the negative density in both the crust (all inversion methods) and mantle (first two inversion methods) at the Tharsis rise. In the Mars model that is used in this study, the mantle plume underneath Tharsis as presented in van der Tang (2021) is used. Either this mantle plume leads to a thinner crust, which is plausible, or this mantle plume is not yet modelled correctly and induces a larger gravity anomaly than is actually present. It might also be a combination of both: a thin crust is present, as well as a slightly overcompensated modelled mantle plume.

This negative density anomaly at the Tharsis rise continues on to Olympus Mons for the first two methods. This opposes the results as presented in van Brummen (2022). Olympus Mons is thought to consist of basaltic rocks, leading to a lower density (2800 kg/m^3 in Delage & Karakostas (2017) and 3000 kg/m^3 in Beuthe et al. (2012)) than the crustal mean (3050 kg/m^3) used in this study, causing this volcano to be large but less heavy than the mean crust. In the results of the third inversion method, Olympus Mons shows a positive density anomaly in both the crust and the mantle. This positive density anomaly in the crust can be due to heavy mantle materials that have erupted, or due to a mean crustal density that is assumed too heavy, implying a high positive density anomaly to compensate for this.

Also, in all crustal maps the density at Olympus Mons is smaller than the mantle density, agreeing to isostasy that the thinner mantle should be able to carry the load on top of it, and thus being heavier than the crustal load.

Then, all the large basins (Hellas, Utopia, Isidis, Argyre), show a positive density anomaly in both the crust and mantle. In the crust, this is expected, while an impact crater has a thin crust, where the mantle material is exposed due to the impact. In the mantle, mostly Hellas basin is very prominent with a high density anomaly. The low topography (and thus shallow crust-mantle boundary) in combination with the high gravity anomaly clearly shows. The impact forming Hellas basin might be so large that material from the lower mantle layers were exposed, leading to a heavier mantle. This result is partially compliant with Ding et al. (2019), who argues the hypothesis that Isidis has a high crustal density, but also that Utopia and Argyre are covered by a low-density sedimentary layer.

In the crust, a clear rim around Utopia is present. Next to the positive density anomaly, a circular negative density anomaly is present. This rim-like feature is seen in impact craters more often and therefore contributes to the conclusion that Utopia is created by an impact.

In the density maps of the first two inversions, a negative density anomaly in the crust at Elysium is present. This feature is also present in the mantle result of the third inversion method, and slightly in the crust. Elysium is a very volcanic region. Therefore, it is not expected that Elysium consists of such a low density crust. It might be the case that the mantle at Elysium is much thinner than this model assumes.

At Valles Marineris, the density anomaly is positive, while it is negative in the results of van Brummen (2022). Valles Marineris is a large canyon that is thought to have formed through a combination of tectonic activity, volcanism and erosion. Sleep (1994) argues that early plate tectonics might be the reason for the origination of the dichotomy. His proposed plate tectonics do not reach all the way to Valles Marineris, however. A more plausible explanation for the positive density anomaly can be that heavier mantle materials erupted due to volcanism, leading to a heavier overall crust material.

In the northern polar region, small patches of higher density anomalies in the crust are visible. These do not appear in the mantle and are not visible in the topography of Mars. These small high anomalies are circular, but distorted due to the Mercator projection. Three larger patches at longitudes 120°, 175° and 190° are present. Potentially, the positive anomalies at 60° and 300° longitude can be counted as well. These smaller positive patches are surrounded by a negative density anomaly. This can lead to the hypothesis of quasi-circular depressions: small, old, impact craters that have been covered by sediment and therefore do not appear on topography maps. However, due to the mantle material exposed underneath this sediment, the crustal density is relatively high. If these patches are indeed QCD's, the crater count of the northern hemisphere could change. This can be a potential piece of evidence for the several impact craters hypothesis for the origination of the dichotomy.

More of these north polar mass enhancements that are smaller than the ones describes in the previous paragraph might exist. However, a limitation of this research is the low resolution of 5° and 10° degrees. Lowering this resolution can allow for smaller features to be determined by this method. Next to this, a higher resolution will also yield a more stable inversion. This is because using the low resolution, the gravity anomaly differences between each of the cells are fairly large. These large differences make it harder for an inversion to converge to the correct result.

Another limitation of this research was that the third inversion method only used the gravitational tensor. This was because the code as we designed it does not incorporate a full matrix of λ with values for each of the gravity components. Incorporating a full λ matrix can make sure that all the different gravity components have their own λ-σ combination that works best for that specific component. Also, it will allow for the decoupling of long ans short wavelength features, as was seen with the other two inversion methods.

References

Aharonson, O., Zuber, M. T., & Rothman, D. H. 2001, Statistics of Mars' topography from the Mars Orbiter Laser Altimeter: Slopes, correlations, and physical models, Journal of Geophysical Research: Planets, 106, 23723

Baratoux, D., Samuel, H., Michaut, C., et al. 2014, Petrological constraints on the density of the Martian crust, Journal of Geophysical Research: Planets, 119, 1707

Belleguic, V., Lognonné, P., & Wieczorek, M. 2005, Constraints on the Martian lithosphere from gravity and topography data, Journal of Geophysical Research: Planets, 110, E11005

Beuthe, M., Maistre, S. L., Rosenblatt, P., Pätzold, M., & Dehant, V. 2012, Density and lithospheric thickness of the Tharsis Province from MEX MaRS and MRO gravity data, Journal of Geophysical Research: Planets, 117, 1

Buczkowski, D. L., Frey, H. V., Roark, J. H., & McGill, G. E. 2005, Buried impact craters: A topographic analysis of quasi-circular depressions, Utopia Basin, Mars, Journal of Geophysical Research: Planets, 110, E03007

Carr, M. H. & Head, J. W. 2010, Geologic history of Mars, Earth and Planetary Science Letters, 294, 185

Comer, R. P., Solomon, S. C., & Head, J. W. 1985, Mars: Thickness of the lithosphere from the tectonic response to volcanic loads, Reviews of Geophysics, 23, 61

Delage, P. & Karakostas, F. 2017, An Investigation of the Mechanical Properties of Some Martian Regolith Simulants with Respect to the Surface Properties at the InSight Mission Landing Site, Space Science Reviews, 211, 191

Ding, M., Lin, J., Gu, C., Huang, Q., & Zuber, M. T. 2019, Variations in Martian Lithospheric Strength Based on Gravity/Topography Analysis, Journal of Geophysical Research: Planets, 124, 3095

Drilleau, M., Samuel, H., Garcia, R. F., et al. 2022, Marsquake Locations and 1-D Seismic Models for Mars From InSight Data, Journal of Geophysical Research: Planets, 127, 1

Durán, C., Khan, A., Ceylan, S., et al. 2022, Seismology on Mars: An analysis of direct, reflected, and converted seismic body waves with implications for interior structure, Physics of the Earth and Planetary Interiors, 325, 106851

Hartmann, W. K. & Neukum, G. 2001, Cratering chronology and the evolution of Mars, Space Science Reviews, 96, 165

Kim, D., Duran, C., Giardini, D., et al. 2023, Global crustal thickness revealed by surface waves orbiting Mars Orbiting Mars, Geophysical Research Letters, 50

Knapmeyer-Endrun, B., Panning, M. P., Bissig, F., et al. 2021, Thickness and structure of the martian crust from InSight seismic data, Science, 373, 2023

Konopliv, A. S., Park, R. S., Rivoldini, A., et al. 2020, Detection of the Chandler Wobble of Mars From Orbiting Spacecraft, Geophysical Research Letters, 47

Liang, F., Yan, J., Zhao, J., Meng, Z., & Barriot, J. P. 2022, Searching for buried craters on Mars based on gravity potential field separation method, Planetary and Space Science, 220, 105532

Martinec, Z. 2014, Mass-density green' functions for the gravitational gradient tensorat different heightsg, Geophysical Journal International, 196, 1455

McGill, G. E. 1989, Buried topography of Utopia, Mars: persistence of a giant impact depression, Journal of Geophysical Research, 94, 2753

McGovern, P. J. 2004, Correction to "Localized gravity/topography admittance and correlation spectra on Mars: Implications for regional and global evolution", Journal of Geophysical Research, 109, E07007

Neumann, G. A., Zuber, M. T., Wieczorek, M. A., et al. 2004, Crustal structure of Mars from gravity and topography, Journal of Geophysical Research: Planets, 109, E08002

Pan, L., Ehlmann, B. L., Carter, J., & Ernst, C. M. 2017, The stratigraphy and history of Mars' northern lowlands through mineralogy of impact craters: A comprehensive survey, Journal of Geophysical Research: Planets, 122, 1824

Pauer, M. & Breuer, D. 2008, Constraints on the maximum crustal density from gravity-topography modeling: Applications to the southern highlands of Mars, Earth and Planetary Science Letters, 276, 253

Qin, W. 2021, Mars Surface Stress Modeling Investigation on the Crustal Structure of Mars with Finite Element Method, Master's thesis, Delft University of Technology

Ritzer, J. A. & Hauck, S. A. 2009, Lithospheric structure and tectonics at Isidis Planitia, Mars, Icarus, 201, 528

Root, B. C., Novák, P., Dirkx, D., et al. 2016, On a spectral method for forward gravity field modelling, Journal of Geodynamics, 97, 22

Sleep, N. H. 1994, Martian plate tectonics, Journal of Geophysical Research, 99, 5639

Sloan, R. K. 1968, Mariner Mars 7964 Project Report: Scientific Experiments

van Brummen, B. 2022, Mars Gravity Inversion Investigating the lateral density variations of the Martian lithosphere, Master's thesis, Delft University of Technology

van der Tang, Y. 2021, The origin of Tharsis - A deep mantle gravity study, Master's thesis, Delft University of Technology

Wieczorek, M. A. 2015, Gravity and Topography of the Terrestrial Planets, Vol. 10 (Elsevier Inc.), 153–193

Wieczorek, M. A., Broquet, A., McLennan, S. M., et al. 2022, InSight Constraints on the Global Character of the Martian Crust, Journal of Geophysical Research: Planets, 127

Wieczorek, M. A. & Zuber, M. T. 2004, Thickness of the Martian crust: Improved constraints from geoid-to-topography ratios, Journal of Geophysical Research: Planets, 109, E01009

Zhong, Z., Yan, J., Liu, X., et al. 2022, The ancient martian lithospheric structure at Isidis Planitia, Icarus, 374, 114741

Zuber, M. T., Solomon, S. C., et al. 2000, Internal structure and early thermal evolution of Mars from MGS topography and gravity, Science, 287, 1788

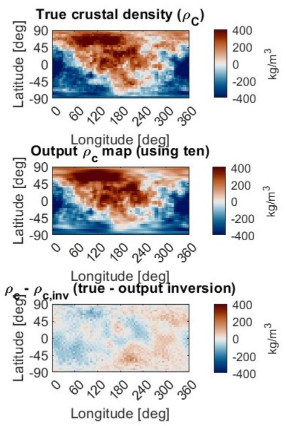

(a) The true crustal density, the output crustal density and the difference between the two.

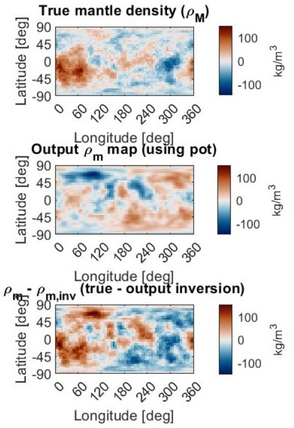

(b) The true mantle density, the output mantle density and the difference between the two.

Fig. A.1: Inversion input and output using synthetic planet 2 and the separated two-layer inversion method.

Appendix A: Synthetic planet 2

This appendix shows the difference in inversion results between the two synthetic planets. The different density profiles are shown in Figure 11a and Figure 11b. Figure A.1 shows the inversion output of the separated two-layer inversion method using the tensor and potential for both layers, but applied to synthetic planet 2. This is the equivalent inversion to Figure A.2, shown in Appendix B, which is the result for synthetic planet 1 (same results as in Figure 12b and Figure 13b, but shown in a different format). The crustal density pattern of synthetic planet 2 is more extreme and therefore results in a better approximation by the inversion. However, from the combination of the results of the crust and mantle, the same conclusions can be drawn as for synthetic planet 1: the crust and mantle show different density outputs, but these are solely based on the error of the previous inversion. The inversion itself is not sensitive to signals from different layers. The hypothesis was that synthetic planet 1 would be easier to invert, as the short and long wavelengths are more separated between the two layers. However, from performing the same inversion on both the synthetic planets it becomes clear that the inversion is not sensitive to the different distributions in the synthetic planets.

Appendix B: Inversion using different gravity components

In Figure A.2, the same results as in the main body of this paper are shown in a different format. These are the results with the separated two-layer inversion method, performed with the gravitational tensor for the crustal inversion and the potential for the mantle inversion. Then, Figure B.1 shows the exact same inversion, but performed with the gravitational vector for both the crust and mantle inversion. Here, one can see that using the same gravity components for both layers results in no decoupling of features at all. Comparing the two inversion settings to each other, it is clear that using the tensor and potential for different layers gives the inversion the chance to put different gravity signals in the crust and mantle layers.

All other combinations of gravity components were tested as well, and the same conclusions can be drawn for those combination. Also, these conclusions hold for all three inversion methods. This enhances the conclusion that incorporating different gravity components in an inversion can lead to better inversion results. Most importantly, different gravity components can attribute different gravity signals to different layers of the interior model.

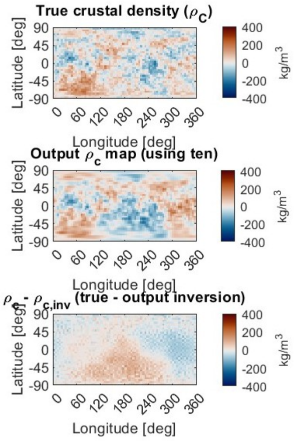

(a) The true crustal density, the output crustal density and the difference between the two

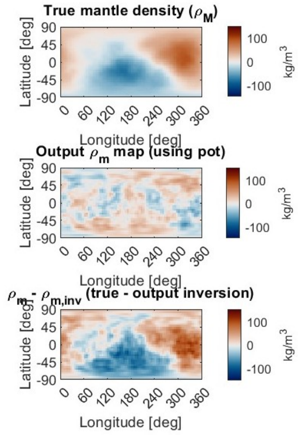

(b) The true mantle density, the output mantle density and the difference between the two.

Fig. A.2: Inversion input and output using synthetic planet 1 and the separated two-layer inversion method, using the gravitational tensor and potential for the inversions of the crust and mantle, respectively.

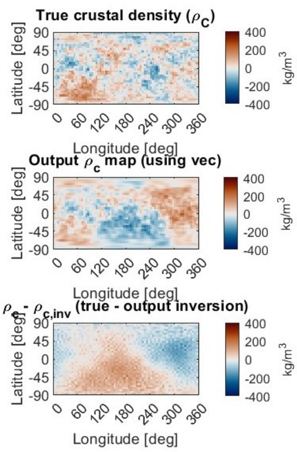

(a) The true crustal density, the output crustal density and the difference between the two.

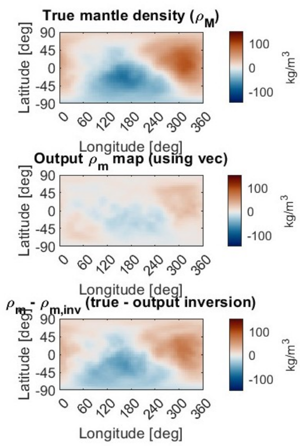

(b) The true mantle density, the output mantle density and the difference between the two.

Fig. B.1: Inversion input and output using synthetic planet 1 and the separated two-layer inversion method, using the gravitational vector for the inversion of both layers.

4

Data analysis and verification and validation

In this chapter, all the data used in the whole study will be discussed. It will be verified and validated, but also analysed. What must be noticed in the data? What are interesting features? How can one data set be visualised and interpreted in different ways? First, the verification and validation is presented. Then, some different analyses are made using the data sets.

4.1. Verification and validation of data sets and tools

The data that is used in this study needs to be verified and validated. Also, the processing of the data needs to be verified. This will be done in this section. First, the topography data from MOLA is elaborated upon. Then, the GSH tool will be discussed. Finally, the gravity data set from MRO is verified and validated.

4.1.1. Martian topography: MOLA

The MOLA instrument on board of the Mars Global Surveyor created a global topography map of Mars. Although this satellite was already launched in 1996, this topography data is still the most advanced. Therefore, the MOLA topography data is used in this research. It can be downloaded from PDS Geosciences[1], where the 4 pixels per degree files are used. This is the data set with the lowest resolution, but due to the gravity data having an even lower resolution (presented in subsection 4.1.3), it is not necessary to use a topography map with a higher resolution.

The topography from MOLA is shown in Figure 4.1a. The dichotomy is clearly visible in the northern lowlands and the southern highlands. This map can be compared to the global topography map in Wieczorek [2015], which is shown in Figure 4.1b. A few differences must be noted: a different color map and a slightly different color bar range are used. Furthermore, the projection and the central meridian (a shift of 90 °) are different. Despite this, it is clear that both maps represent the same topography pattern. Slight differences originate from the difference between the MOLA data set and the MarsTopo2600 map as used by Wieczorek [2015]. MarsTopo2600 is a shape file that can be obtained from Zenodo[2] and contains the flattening of Mars. This is a difference in spherical harmonic degree 2.

From Figure 4.1 it is clear that the MOLA data was processed correctly. Therefore, this part of the data is verified. Validation already was presented in Wieczorek [2015].

[1]`https://pds-geosciences.wustl.edu/missions/mgs/megdr.html`, last accessed on 29 August 2023
[2]`https://zenodo.org/record/3870922`, last accessed on 29 August 2023

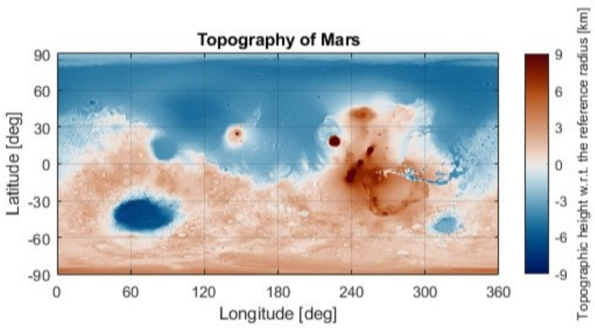

(a) Topography of Mars using MOLA data.

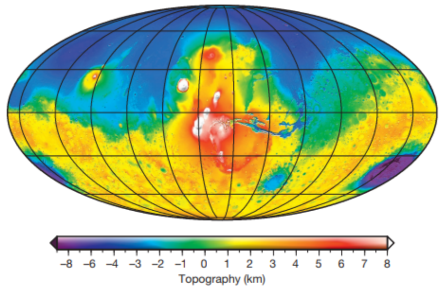

(b) Topography of Mars as presented in Wieczorek [2015], which uses MarsTopo2600

Figure 4.1: Validation of MOLA data with Wieczorek [2015]

4.1.2. GSH tool

The MRO120F data set is processed using the Global Spherical Harmonic (GSH) tool defined by Root et al. [2016], consisting of GSHA and GSHS. The Global Spherical Harmonic Analysis (GSHA) code analyses the planet layer by layer, converting each layer into a set of spherical harmonic coefficients to retrieve the spherical harmonic representation. This set of spherical harmonics can be translated by the Global Spherical Harmonic Synthesis (GSHS) to calculate the grids of the gravity vectors, gravitational potential and tensor fields. This toolbox is not only used to process the MRO120F data, but also to derive the gravity field of the obtained density variations after inversion.

In Root et al. [2016] this toolbox is validated for the Earth. However, it can be adapted to other planets. Changing the input model and the other planet-specific parameters to Mars make this GSH toolbox applicable to this planet. This is presented as well in de Backer [2018]. As this toolbox has been verified and validated by these sources and the toolbox will be used as-is, a separate validation is not presented in this thesis. However, in section 4.2 and section 4.3 the GSH tool will be applied to the topography and gravity data, such that my implementation of the tool is verified.

4.1.3. Martian gravity: a comparison of different data sets

The newest gravity data set of Mars is MRO120F [Konopliv et al., 2020], this is the follow-up on MRO120D. This data set uses data from Mars Reconnaissance Orbiter, with small additions of other satellites like MGS. NASA created another data set, GMM-3, from the same data of MRO. These three data sets are all commonly used in research. In order to determine which one will be used in this thesis research, Figure 4.2 is presented. From this figure, it is evident that the degree variance of all three data sets are very similar, especially up until degree 90. It is also clear that the MRO120F data set has a smaller error than the MRO120D data set. Also, although GMM-3 has an even lower error at the smaller degrees, its error is larger then both MRO120 data sets from spherical harmonic degree 40 onward. As this research will not only focus on larger wavelengths features, the higher degrees are just as important as the smaller degrees. Thus, MRO120F is preferred due to its smaller error than MRO120D and smaller error in the higher degrees than GMM-3. In order to validate the data, it is compared to the degree variance as presented in literature. First of all, the degree variance of MRO120D and MRO120F and GMM-3 are presented in Figure 4.2. This can be compared to the degree variance of MRO120D as presented in Gorski et al. [2018] and the degree variance of GMM-3 as presented in Genova [2020]. It can be visually inspected that both the MRO120D as well as the GMM-3 data set are the same as presented in literature. Therefore, the conclusion is drawn that this data is correctly processed.

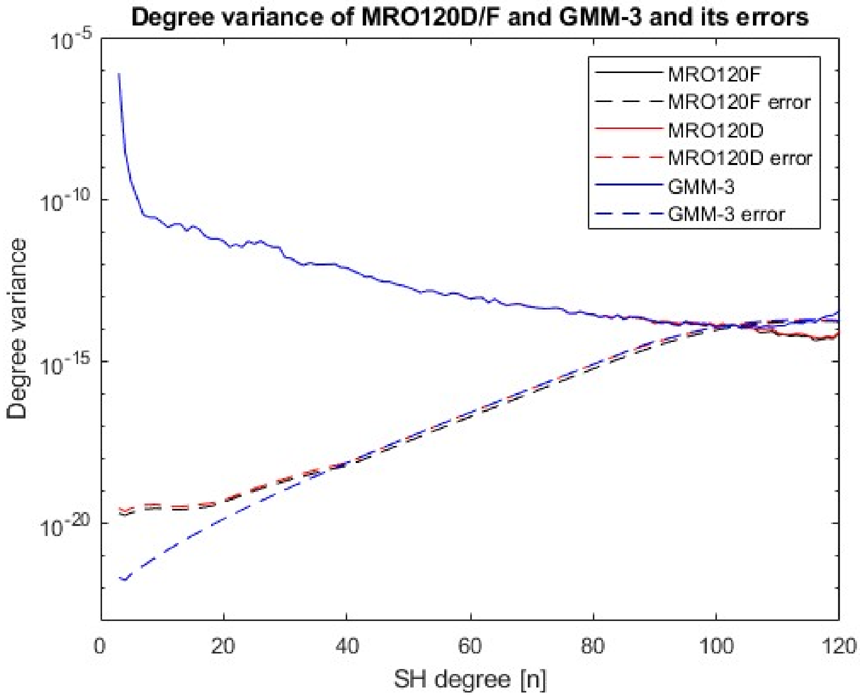

Figure 4.2: Degree variance of MRO120F, MRO120D and GMM-3, including their respective errors

However, by this MRO120F is not yet validated. MRO120F was developed by Konopliv et al. [2020] in which it is also validated. The processing of MRO120F was done in the same way as MRO120D. As MRO120D has been verified in the previous paragraph, it is concluded that the processing of MRO120F was also performed correctly. Therefore, the MRO120F data set and its processing has been verified and validated.

Zooming in on Figure 4.2, Figure 4.3 is produced. It is clear that the error of MRO120F stays lower than MRO120D and GMM-3 all the way up until degree 120. It can be observed that the actual signal of MRO120F is larger than its error until degree 103, after which the error gets larger than the signal. Therefore, the data after degree 103 should not be used in the research. However, one can consider to already cut off the data earlier, in order to ensure that the signal is not influenced significantly by the error. Most research (e.g. [van Brummen, 2022], [Qin, 2021]) cut off the data already at spherical harmonic degree 90. In this research this will also be done.

4.2. Vertical gravity gradient and anomaly

Using MRO120F and the GSH toolbox, the vertical gravity gradient of Mars is visualised. This is done at a height of 0 km and up to and including spherical harmonic degree 90. Figure 4.4a shows the gravity gradient, from which it is clear that the mean gravity is indeed around 3.72 m/s^2, as was also presented in the introduction. It is also clear that there is some large wavelength feature present: the flattening of Mars. In order to get a better idea of the gravity anomalies due to topography and the interior of Mars, the gravity is corrected for the mass of the planet (spherical harmonic coefficient C00) and the flattening of Mars (C20). Additionally, the data is corrected for the terms C10, C11 and S11, which dictate the center of mass of the planet. It must be noted, however, that when using MRO120F these are already zero. This is due to the fact that its data is defined to be coinciding with the actual center of mass of Mars. The gravity anomaly corrected for the previously named terms is shown in Figure 4.4b. This gravity anomaly originates from differences in topography and interior structures. Interesting

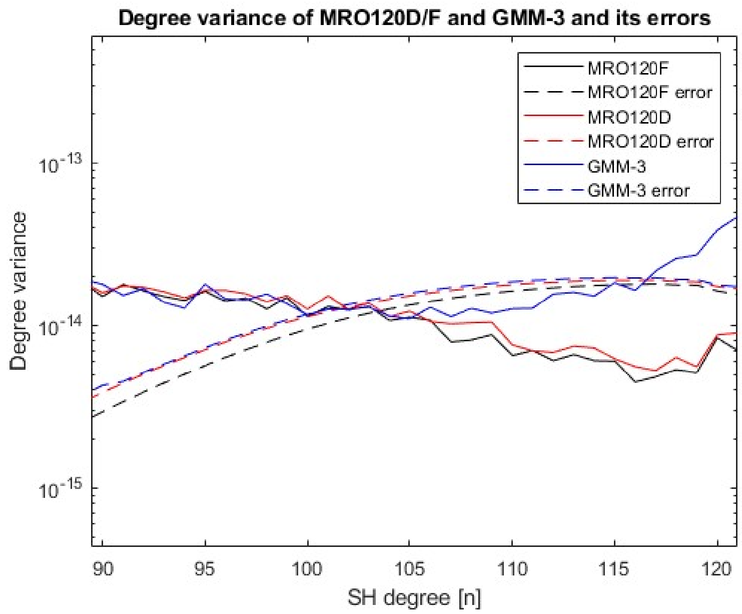

Figure 4.3: Zoomed in version of Figure 4.2, showing the higher degree values for all three data sets.

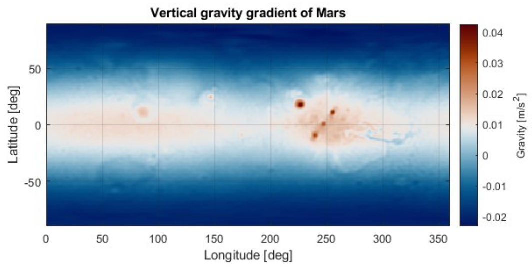

(a) The vertical gravity gradient of Mars

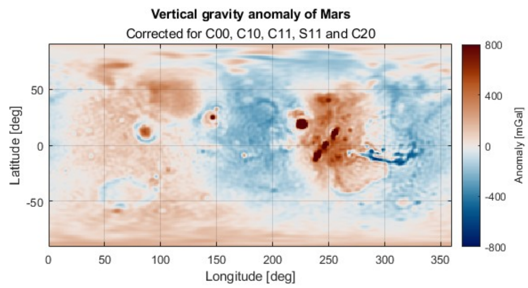

(b) Gravity anomaly of Mars. Note that the color bar has been cut off and that the actual minimum is -718 mGal and the actual maximum is 3461 mGal.

Figure 4.4: Vertical gravity gradient and anomaly of Mars using MRO120F

points in this figure are the high anomalies at Olympus Mons and the negative rings around positive anomalies in several basins, like Hellas.

To verify that, again, this data is processed correctly it can be compared to a vertical gravity gradient map, also corrected for these terms, of MRO120D. This is shown in Figure 4.5. It is clear that both resemble each other very well. Small differences might be distinguished. These can be explained by the small difference between MRO120D and MRO120F, which were already presented in subsection 4.1.3.

4.3. Bouguer anomaly

The gravity anomaly as presented in section 4.2 originates from both topographic as well as subsurface features. As this thesis research focuses on subsurface structures, the anomaly due to topography should be subtracted. This is the so-called Bouguer correction. The Bouguer correction can be performed in two ways: the simple (analytic) Bouguer correction and the extended (non-analytic) Bouguer correction, performed using the GSH tool. Both will be presented in this section.

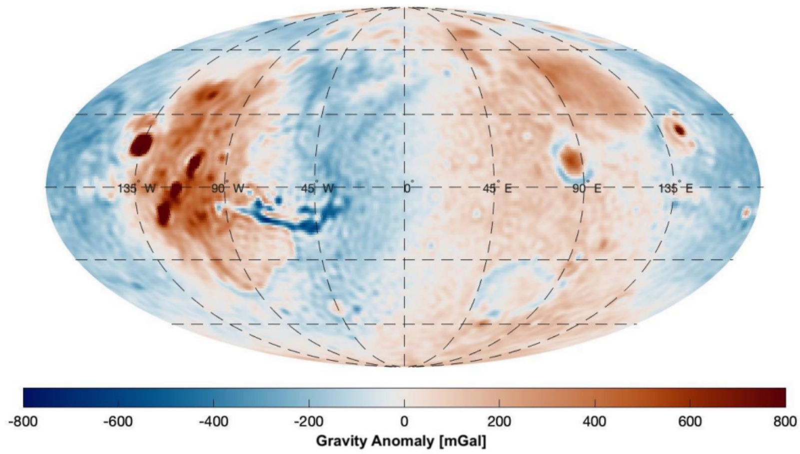

Figure 4.5: Gravity anomaly of Mars, corrected for C00, C10, C11, S11 and C20 as presented by van Brummen [2022]. It must be noted that both the projection and the central meridian are different. The color map and color bar used is the same.

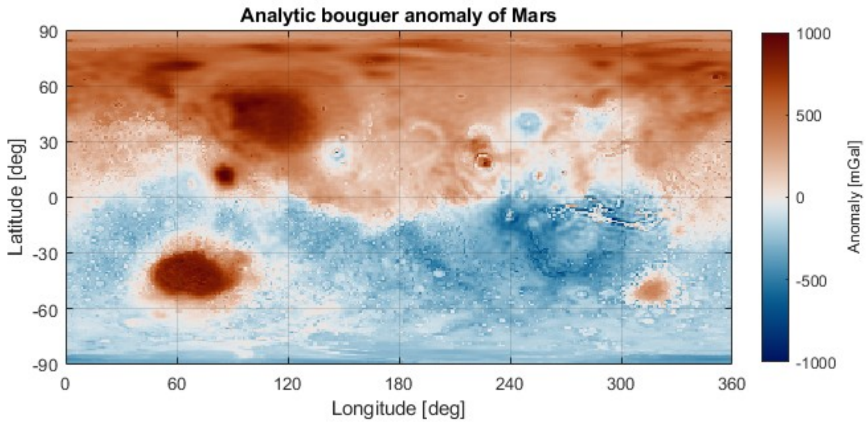

Figure 4.6: Analytic Bouguer anomaly with a maximum of 1036 mGal and a minimum of -945 mGal

4.3.1. Analytic Bouguer anomaly

The simple (analytic) Bouguer anomaly is calculated by subtracting the Bouguer correction from the full gravity anomaly. This is presented in the following equation:

$$g_B = g_{FA} - \delta g_B, \tag{4.1}$$

in which g_B is the Bouguer anomaly, g_{FA} the free-air anomaly or the gravity anomaly as presented in Figure 4.4b and δg_B the Bouguer correction. The Bouguer correction can be approximated using

$$\delta g_B = 2\pi G \rho h, \tag{4.2}$$

in which G is the gravitational constant, ρ the crustal density and h the topography. In this calculation, the crustal density is assumed to be constant at a value of 3050 kg/m^3. The MOLA topography as elaborated upon in subsection 4.1.1 is used. This produces Figure 4.6. The Bouguer anomaly shows higher values than the gravity anomaly itself, as the influence of topography is removed and compensation and isostasy reveal their strength. The dichotomy is clearly present: due to the low topography in the north the Bouguer anomaly is fairly high.

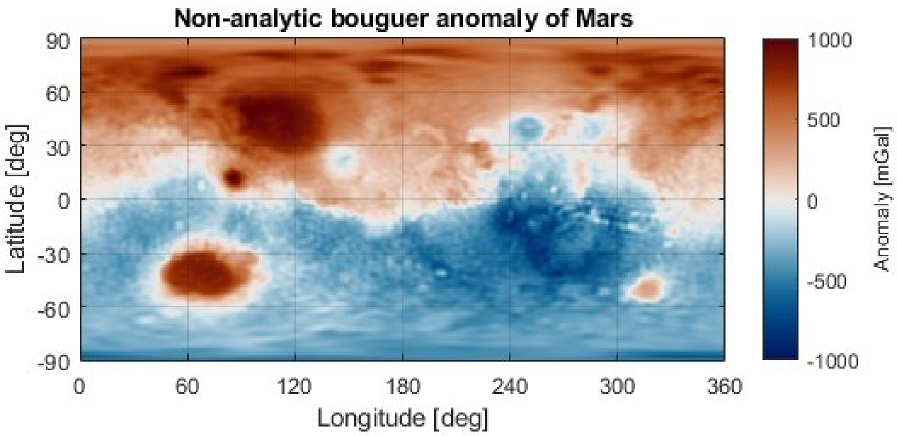

Figure 4.7: Non-analytic Bouguer anomaly with a maximum of 1064 mGal and a minimum of -931 mGal

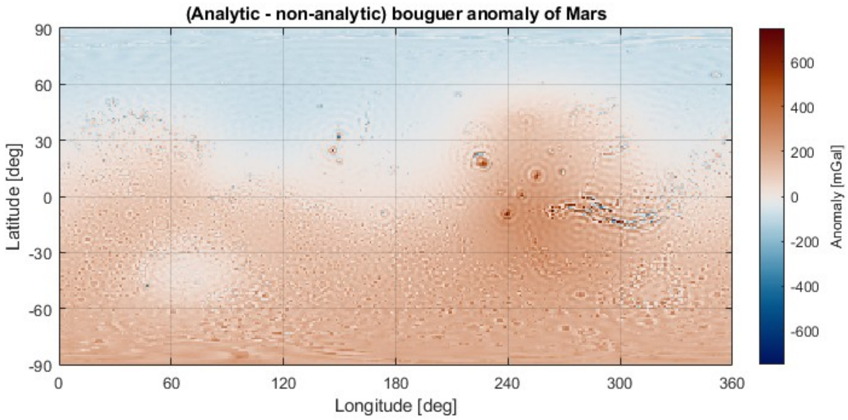

Figure 4.8: Difference between the analytic and the non-analytic Bouguer anomalies with a maximum of 793 mGal and a minimum of -657 mGal

4.3.2. Non-analytic Bouguer anomaly

The analytic Bouguer anomaly is simply an approximation of the real Bouguer anomaly. Using the GSH tool in Matlab, a more accurate Bouguer anomaly can be computed. Using an input model of just the topography layer, the gravitational signal due to this layer can be calculated using GSHA. Then, this spherical harmonic gravity data can be synthesized to an actual grid using GSHS. This spatial grid is the gravity anomaly purely due to topography.

Then, this topographic gravity anomaly can be subtracted from the full, corrected gravity anomaly as presented in Figure 4.4b. This is shown in Figure 4.7. It is clear that the same features as in Figure 4.6 are present and that the maximum and minimum values are very similar. It can therefore be concluded that the two ways of computing the Bouguer anomaly are correct and verified. However, it is interesting to create a map of the difference of the two Bouguer anomalies. This map is plotted in Figure 4.8. Two main interesting things are happening. The first one is the dichotomy that is showing. Apparently, the analytic Bouguer correction can not fully grasp the implication of such a distinct topography pattern. This is mainly due to the assumption of the analytic Bouguer correction that each element is modelled as an infinite plate, instead of part of a 3D sphere. As the dichotomy is a large features that spans the whole 3D planet, the infinite plate assumption has a large influence on the result. Secondly, the highest difference is at Olympus Mons and the Tharsis region. As the topography has a very high gradient at those locations, the analytic Bouguer correction can not compensate

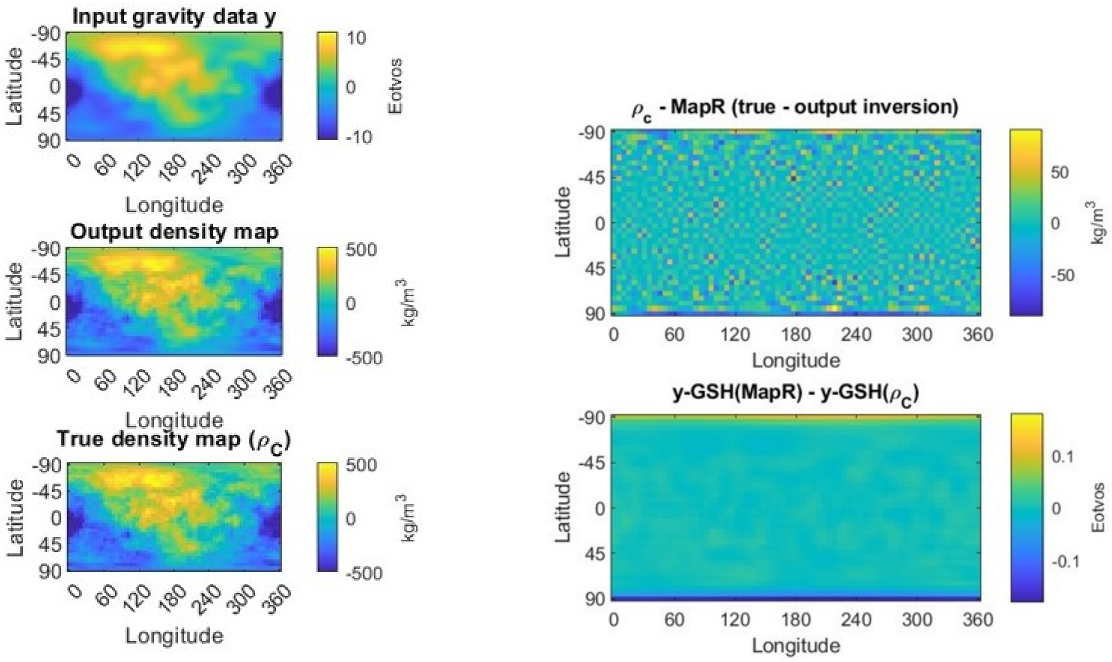

(a) The middle figure shows the output after a one layer inversion, using the input from the top figure. The bottom figure shows the true density anomalies.

(b) The errors arising after the inversion. The top figure shows the density errors. The bottom figure shows the gravity error, being the difference between the true (input) gravity and the output gravity resulting from the output density map.

Figure 4.9: Results of a one-layer inversion after only one iteration.

for this steep terrain as good as the GSH tool can.

4.4. One-layer inversion

In section 2.3 it was explained that a one-layer inversion is used for the sensitivity analysis. Here, the one-layer inversion is discussed. Figure 4.9 shows the input and output of a one-layer inversion. This one-layer inversion is performed using the optimal combination of λ, σ and height as presented in Table 2.1, using the gravitational tensor. Only one iteration is performed. From Figure 4.9b it can be concluded that already after one iteration, all geological features presented by the gravity residual are incorporated in the density anomaly map. This means that the one-layer inversion is capable of attributing the correct density anomalies to the gravity residual. In this one-layer inversion, the topography, crust-mantle boundary and density map of the bottom layer are constrained, leaving only the density map of the crustal layer to be determined by the gravity residual. Combining the analysis as performed in section 2.3 and this result, it can be concluded that a one-layer inversion is capable of correctly determining all density anomalies of the inverted layer.

5 Conclusions and recommendations

This chapter is supplementing the conclusions and discussion as presented in the journal article (Chapter 3). As this thesis report elaborates on the one-layer inversion that was performed before the two-layer inversion, conclusions on that will be drawn in section 5.1. Then, recommendations and next steps to improve the method of inversion are presented in section 5.2.

5.1. Conclusions

The conclusions from the journal article focused on the geological interpretations of the Martian crustal and mantle density profiles. With respect to the inversion methods, the main conclusion was that different gravity components allow for a decoupling between long and short wavelengths, and that the combined dependent inversion method was able to attribute gravity signals into different layers. A combination of both would increase the accuracy of the inversion. Next to these conclusions, conclusions can be drawn on the parts of the research that are only presented in the thesis supporting the journal article.

The first conclusion on the preliminary research on the λ-σ combination, as presented in section 2.3, is that the optimal combination between these two parameters is a linear relationship, where the gravity component has an effect on the relative strength of λ compared to σ. The optimal height of the observations is also specific to the gravity component. This conclusion can be implemented in further research using gravity inversion.

The second conclusion on the preliminary study on the one-layer inversion, is that the most important parameter of the interior model is the depth of the layer. If this parameter is estimated correctly, the results of the inversion improve drastically. Other interior parameters like the crust-mantle boundary and the elastic lithospheric thickness are less important. This leads to the conclusion that the focus should be to incorporate the correct layer depth in the interior model.

Next to the conclusions on the two-layer model as presented in the journal article, it is interesting to further look at the combined dependent two-layer inversion. This inversion only uses one gravity component, while it is already concluded that incorporating multiple gravity components allow for a decoupling of long and short wavelengths. This leads to the conclusion that a full gravity component matrix will enhance the results. In section 5.2, this will be elaborated upon.

Going back to the research question as defined in section 1.4: *How can subsurface density variations be obtained by a two-layer gravity inversion, in order to better understand Martian surface features and their geological history?* The answer to the question is formulated as follows: the combined dependent two-layer inversion method should be combined with the use of multiple gravity components, where the combination of λ and σ, the height of the satellite observations and the depth of the respective layers should be carefully chosen.

5.2. Recommendations

We recommend that the next research uses the third inversion method. Several recommendations applying to this inversion method can be made.

The sensitivity analysis that we performed on the optimal λ-σ combinations and height, is performed on a two-layer model, but a one-layer inversion. When working with the two-layer inversion, it was evident that these optimal combinations were not one-to-one applicable anymore. Especially, the value of λ turned out to be even more susceptible to changes. Two orders of magnitude could make a difference between not converging at all and large edge effects. Therefore, a separate analysis of the Tikhonov parameter could be made specifically for the third inversion method.

Secondly, due to running time the third inversion method was limited to a resolution of 10 degrees, while the gravity data of Mars is available in a higher resolution. Rewriting the code, using a server with a high computational load or simply letting the code run for longer can lead to being able to use a smaller resolution. Using a smaller resolution not only more details are visible in the result, but also the inversion will be more stable. This is because using the low resolution, the gravity anomaly differences between each cell are fairly large. These large differences make it harder for an inversion to converge to the correct result.

A third recommendation is to look into a way of incorporating a full λ matrix. In this research, only one value for λ was used and the weights of each gravity component were adjusted accordingly. However, as mentioned in the first recommendation, the value of λ was more sensitive to the different gravity components than the one-layer inversion. Therefore, it turned out that each gravity component needed a different value of λ for a stable inversion. Incorporating a full λ matrix can make sure that all the different gravity components have their own λ-σ combination that works best for that specific component. Thus, leading to a more reliable inversion.

When all these recommendations are implemented, a final limitation might be the resolution of the available gravity data. In this research, data up until spherical harmonic degree 90 was used. If the resolution of the inversion itself is indeed higher (as proposed by the first recommendation), it might be that the gravity observation data can not reach the same resolution. Spherical harmonic degree 90 agrees to surface features of a few hundred kilometers. It might be that the small northern mass anomalies as seen in the crustal density maps of Mars might not be the only potential impact basins: more smaller ones might exist. However, using this method and data set these potential smaller features are not visible.

Bibliography

O. Aharonson, M. T. Zuber, and D. H. Rothman. Statistics of mars' topography from the mars orbiter laser altimeter: Slopes, correlations, and physical models. *Journal of Geophysical Research: Planets*, 106:23723–23735, 10 2001. doi: 10.1029/2000JE001403.

D. Baratoux, H. Samuel, C. Michaut, et al. Petrological constraints on the density of the martian crust. *Journal of Geophysical Research: Planets*, 119:1707–1727, 2014. doi: 10.1002/2014JE004642.

V. Belleguic, P. Lognonné, and M. Wieczorek. Constraints on the martian lithosphere from gravity and topography data. *Journal of Geophysical Research: Planets*, 110:E11005, 11 2005. doi: 10.1029/2005JE002437.

A. Broquet and J. Andrews-Hanna. Geophysical evidence for an active mantle plume underneath elysium planitia on mars. *Nature astronomy*, 7:160–169, 2022.

D. L. Buczkowski, H. V. Frey, J. H. Roark, and G. E. McGill. Buried impact craters: A topographic analysis of quasi-circular depressions, utopia basin, mars. *Journal of Geophysical Research: Planets*, 110:E03007, 3 2005. doi: 10.1029/2004JE002324.

M. H. Carr and J. W. Head. Geologic history of mars. *Earth and Planetary Science Letters*, 294: 185–203, 6 2010. doi: 10.1016/j.epsl.2009.06.042.

L. de Backer. Seismic analysis of mars using gravita-tional potential stresses-insight. Master's thesis, Delft University of Technology, 2018.

M. Ding, J. Lin, C. Gu, Q. Huang, and M. T. Zuber. Variations in martian lithospheric strength based on gravity/topography analysis. *Journal of Geophysical Research: Planets*, 124:3095–3118, 11 2019. doi: 10.1029/2019JE005937.

L. T. Elkins-Tanton, E. M. Parmentier, and P. C. Hess. Magma ocean fractional crystallization and cumulate overturn in terrestrial planets: Implications for mars. *Meteoritics and Planetary Science*, 38:1753–1771, 2003. doi: 10.1111/j.1945-5100.2003.tb00013.x.

A. Ermakov, R. Park, and B. Bills. Power laws of topography and gravity spectra of the solar system bodies. *Journal of Geophysical research: Planets*, 123:2038–2064, 2018. doi: 10.1029/RG001i004p00507.

H. Frey and R. A. Schultz. Large impact basins and the mega-impact origin for the crustal dichotomy on mars. *Geophysical Research Letters*, 15:229–232, 1988. doi: 10.1029/GL015i003p00229.

H. V. Frey and R. A. Schultz. Speculations on the origin and evolution of the utopia-elysium lowlands of mars. *Journal of Geophysical Research*, 95, 1990. doi: 10.1029/jb095ib09p14203.

A. Genova. Oracle: A mission concept to study mars' climate, surface and interior. *Acta Astronautica*, 166:317–329, 1 2020. doi: 10.1016/j.actaastro.2019.10.006.

K. M. Gorski, B. G. Bills, and A. S. Konopliv. A high resolution mars surface gravity grid. *Planetary and Space Science*, 160:84–106, 10 2018. doi: 10.1016/j.pss.2018.03.015.

P. C. Hansen. *The L-curve and its use in the numerical treatment of inverse problems*. WIT Press, 2001.

W. M. Kaula. Determination of the earth's gravitational field. *Reviews of Geophysics*, 1:507–551, 1963. doi: 10.1029/RG001i004p00507.

A. Khan, S. Ceylan, M. V. Driel, et al. Upper mantle structure of mars from insight seismic data. *Science*, 373:434–438, 2021. URL `https://www.science.org`.

D. Kim, C. Duran, D. Giardini, et al. Global crustal thickness revealed by surface waves orbiting mars orbiting mars. *Geophysical Research Letters*, 50, 2023. doi: 10.22541/essoar.167810298.85030230/v1. URL `https://doi.org/10.22541/essoar.167810298.85030230/v1`.

B. Knapmeyer-Endrun, M. P. Panning, F. Bissig, et al. Thickness and structure of the martian crust from insight seismic data. *Science*, 373:2023, 2021. URL `https://www.science.org`.

A. S. Konopliv, R. S. Park, A. Rivoldini, R. M. Baland, S. L. Maistre, T. V. Hoolst, M. Yseboodt, and V. Dehant. Detection of the chandler wobble of mars from orbiting spacecraft. *Geophysical Research Letters*, 47, 11 2020. doi: 10.1029/2020GL090568.

F. Liang, J. Yan, J. Zhao, Z. Meng, and J. P. Barriot. Searching for buried craters on mars based on gravity potential field separation method. *Planetary and Space Science*, 220:105532, 10 2022. doi: 10.1016/j.pss.2022.105532.

Z. Martinec. Mass-density green' functions for the gravitational gradient tensorat different heightsg. *Geophysical Journal International*, 196:1455–1465, 3 2014. doi: 10.1093/gji/ggt495.

G. E. Mcgill and S. W. Squyres. Origin of the martian crustal dichotomy" evaluating hypotheses. *ICARUS*, 93:386–393, 1991.

P. J. McGovern. Correction to "localized gravity/topography admittance and correlation spectra on mars: Implications for regional and global evolution". *Journal of Geophysical Research*, 109: E07007, 2004. doi: 10.1029/2004je002286.

P. Mouginis-Mark. Olympus mons volcano, mars: A photogeologic view and new insights. *Chemie der Erde*, 78:397–431, 12 2018. doi: 10.1016/j.chemer.2017.11.006.

J. Mussini. An anisotropic flexural isostasy method for investigating the martian lithosphere. Master's thesis, Delft University of Technology, 2020. URL `http://repository.tudelft.nl/`.

G. A. Neumann, M. T. Zuber, M. A. Wieczorek, P. J. McGovern, F. G. Lemoine, and D. E. Smith. Crustal structure of mars from gravity and topography. *Journal of Geophysical Research: Planets*, 109:E08002, 8 2004. doi: 10.1029/2004JE002262.

M. Pauer and D. Breuer. Constraints on the maximum crustal density from gravity-topography modeling: Applications to the southern highlands of mars. *Earth and Planetary Science Letters*, 276:253–261, 12 2008. doi: 10.1016/j.epsl.2008.09.014.

R. J. Philips, M. T. Zuber, S. C. Solomon, et al. Ancient geodynamics and global-scale hydrology on mars. *Science*, 291:2584–2587, 3 2001. doi: 10.1126/science.1056374.

R. J. Phillips, M. T. Zuber, S. E. Smrekar, et al. Mars north polar deposits: Stratigraphy, age, and geodynamical response. *Science*, 2008. URL `https://www.science.org`.

W. Qin. Mars surface stress modeling investigation on the crustal structure of mars with finite element method. Master's thesis, Delft University of Technology, 2021. URL `http://repository.tudelft.nl/`.

J. A. Ritzer and S. A. Hauck. Lithospheric structure and tectonics at isidis planitia, mars. *Icarus*, 201:528–539, 6 2009. doi: 10.1016/j.icarus.2009.01.025.

B. Root. Lecture notes on planetary gravity field modelling. 2021.

B. C. Root, P. Novák, D. Dirkx, et al. On a spectral method for forward gravity field modelling. *Journal of Geodynamics*, 97:22–30, 12 2016. doi: 10.1016/j.jog.2016.02.008.

E. J. O. Schrama. Lecture notes on planetary sciences and satellite orbit determination. 2020.

N. H. Sleep. Martian plate tectonics. *Journal of Geophysical Research*, 99:5639–5655, 1994. doi: 10.1029/94JE00216.

N. H. Sleep and R. J. Phillips. Gravity and lithospheric stress on the terrestrial planets with reference to the tharsis region of mars. *Journal of Geophysical Research: Solid Earth*, 90: 4469–4489, 5 1985. doi: 10.1029/jb090ib06p04469.

S. E. Smrekar, P. Lognonné, T. Spohn, et al. Pre-mission insights on the interior of mars. *Space Science Reviews*, 215, 1 2019. doi: 10.1007/s11214-018-0563-9.

S. C. Solomon, O. Aharonson, J. M. Aurnou, et al. New perspectives on ancient mars. *Science*, 2001. URL `www.sciencemag.org`.

K. L. Tanaka and G. J. Leonard. Geology and landscape evolution of the hellas region of mars. *Journal of Geophysical Research*, 100:5407–5432, 1995. doi: 10.1029/94JE02804.

B. van Brummen. Mars gravity inversion investigating the lateral density variations of the martian lithosphere. Master's thesis, Delft University of Technology, 2022. URL `http://repository.tudelft.nl/`.

Y. van der Tang. The origin og tharsis - a deep mantle gravity study. Master's thesis, Delft University of Technology, 2021.

A. B. Watts and J. D. Moore. Flexural isostasy: Constraints from gravity and topography power spectra. *Journal of Geophysical Research: Solid Earth*, 122:8417–8430, 10 2017. doi: 10.1002/2017JB014571.

M. A. Wieczorek. *Gravity and Topography of the Terrestrial Planets*, volume 10. Elsevier Inc., 1 2015. ISBN 9780444538031. doi: 10.1016/B978-0-444-53802-4.00169-X.

M. A. Wieczorek and F. J. Simons. Localized spectral analysis on the sphere. *Geophysical Journal International*, 162:655–675, 9 2005. doi: 10.1111/j.1365-246X.2005.02687.x.

M. A. Wieczorek and M. T. Zuber. Thickness of the martian crust: Improved constraints from geoid-to-topography ratios. *Journal of Geophysical Research: Planets*, 109:E01009, 1 2004. doi: 10.1029/2003je002153.

M. A. Wieczorek, A. Broquet, S. M. McLennan, et al. Insight constraints on the global character of the martian crust. *Journal of Geophysical Research: Planets*, 127, 5 2022. doi: 10.1029/2022JE007298.

D. E. Wilhelms and S. W. Squyres. The martian hemispheric dichotomy may be due to a giant impact. *Nature*, 309:138–140, 1984.

D. Williams. Mars fact sheet. 2004.

Z. Zhong, J. Yan, X. Liu, et al. The ancient martian lithospheric structure at isidis planitia. *Icarus*, 374:114741, 3 2022. doi: 10.1016/j.icarus.2021.114741.

M. T. Zuber, S. C. Solomon, et al. Internal structure and early thermal evolution of mars from mgs topography and gravity. *Science*, 287:1788–1793, 2000.